Senescent cells develop PDK4-dependent hypercatabolism and produce lactate to promote cancer resistance and aging

Xuefeng Dou
Chinese Academy of Science
Qiang Fu
Binzhou Medical University https://orcid.org/0000-0002-6932-7103
Qilai Long
Fudan University
Shuning Liu
East China University of Science and Technology
Yejun Zou
State Key Laboratory of Bioreactor Engineering, School of Pharmacy, East China University of Science and Technology
Da Fu
Shanghai Jiao Tong University School of Medicine
Qixia Xu
Chinese Academy of Sciences
Zhirui Jiang
Chinese Academy of Sciences
Xiaohui Ren
Chinese Academy of Sciences
Guilong Zhang
Binzhou Medical University
Xiaoling Wei
Fudan University
Qingfeng Li
Shanghai Ninth People's Hospital, Shanghai Jiao Tong University School of Medicine
https://orcid.org/0000-0001-7822-618X
Judith Campisi
Buck Institute https://orcid.org/0000-0001-6858-9462
Yuzheng Zhao
East China University of Science and Technology https://orcid.org/0000-0001-5400-0135
Yu Sun (sunyu@sibs.ac.cn)

Chinese Academy of Sciences https://orcid.org/0000-0001-7121-9112

Article

Keywords:

Posted Date: January 27th, 2023

DOI: https://doi.org/10.21203/rs.3.rs-2485584/v1

Additional Declarations: There is **NO** Competing Interest.

Version of Record: A version of this preprint was published at Nature Metabolism on October 30th, 2023. See the published version at https://doi.org/10.1038/s42255-023-00912-w.

Senescent cells develop PDK4-dependent hypercatabolism and produce lactate to promote cancer resistance and aging

Xuefeng Dou[1,14], Qiang Fu[2,14], Qilai Long[3,14], Shuning Liu[4], Yejun Zou[4,5], Da Fu[6], Qixia Xu[1], Zhirui Jiang[1], Xiaohui Ren[1], Guilong Zhang[2,7], Xiaoling Wei[8,9], Qingfeng Li[10], Judith Campisi[11,12], Yuzheng Zhao[4,5,*] and Yu Sun[1,2,13,*]

Author affiliations

1. Key Laboratory of Tissue Microenvironment and Tumor, Shanghai Institute of Nutrition and Health, University of Chinese Academy of Sciences, Chinese Academy of Sciences, Shanghai 200031, China
2. Department of Pharmacology, Institute of Aging Medicine, Binzhou Medical University, Yantai, Shandong 264003, China
3. Department of Urology, Zhongshan Hospital, Fudan University, Shanghai 200032, China
4. Optogenetics & Synthetic Biology Interdisciplinary Research Center, State Key Laboratory of Bioreactor Engineering, Shanghai Frontiers Science Center of Optogenetic Techniques for Cell Metabolism, School of Pharmacy, East China University of Science and Technology, Shanghai 200237, China
5. Research Unit of New Techniques for Live-cell Metabolic Imaging, Chinese Academy of Medical Sciences, Beijing 100730, China
6. Department of General Surgery, Pancreatic Disease Institute, Ruijin Hospital, Shanghai Jiao Tong University School of Medicine, Shanghai 200025, China
7. Department of Pharmacology, Shandong Technology Innovation Center of Molecular Targeting and Intelligent Diagnosis and Treatment, Binzhou Medical University, Yantai, 264003, China
8. Department of Endodontics, Shanghai Stomatological Hospital and School of Stomatology, Fudan University, Shanghai, China
9. Shanghai Key Laboratory of Craniomaxillofacial Development and Diseases, Fudan University, Shanghai, China
10. Department of Plastic & Reconstructive Surgery, Shanghai Ninth People's Hospital, Shanghai Jiao

Tong University School of Medicine, Shanghai 200011, China

11. Buck Institute for Research on Aging, Novato, CA 94945, USA

12. Lawrence Berkeley National Laboratory, University of California, Berkeley, CA 94720, USA

13. Department of Medicine and VAPSHCS, University of Washington, Seattle, WA 98195, USA

14. These authors contributed equally: Xuefeng Dou, Qiang Fu, Qilai Long.

* Correspondence: yuzhengzhao@ecust.edu.cn; sunyu@sibs.ac.cn

Abstract

Senescent cells remain metabolically active, but their metabolic landscape and resulting implications remain underexplored. Here we highlight upregulation of pyruvate dehydrogenase kinase 4 (PDK4) upon cellular senescence, a tendency adversely correlated with cancer patient survival after chemotherapy. Senescent cells exhibit increased aerobic glycolysis and enhanced lactate production, but subject to reversal upon PDK4 inhibition. Distinct from the cancer cell-featured Warburg effect, however, senescent cells sustain mitochondrial respiration and redox activity, adopting a special form of metabolic reprogramming. Media from PDK4$^+$ stromal cells change global expression and promote malignancy of recipient cancer cells *in vitro*, while targeting PDK4 causes tumor regression *in vivo*. The metabolite lactate causes NOX1 upregulation and ROS production in mitochondrion-disabled cells, whereas PDK4 suppression reduces DNA damage severity and restrains the senescence-associated secretory phenotype (SASP). In preclinical trials, PDK4 intervention alleviates physical dysfunction and prevents age-associated frailty, conditions frequently observed in advanced life. Together, our study substantiates the hypercatabolic nature of senescent cells, and reveals a metabolic link between cellular senescence, lactate production, chronological aging and age-related pathologies including but not limited to cancer.

Introduction

Cellular senescence was initially identified as a program characterized with loss of proliferative capacity after exhaustive passaging in culture, which is known as replicative senescence (RS) [1]. Later studies demonstrated that senescence is indeed inducible by multiple types of inherent or environmental stresses, including oncogenic activation (oncogene-induced senescence, OIS) or therapeutic insults (therapy-induced senescence, TIS) [2]. Senescent cells exhibit phenotypic alterations, such as morphological flattening, nuclear expansion, epigenetic reorganization and metabolic alterations [3, 4]. They also display cell non-autonomous activities, particularly chronic secretion of numerous pro-inflammatory cytokines and chemokines, a phenotype termed the SASP [5]. The SASP plays a context-dependent role in organismal aging and diverse age-related disorders [4]. The net effect of the SASP is mostly detrimental in advanced life stages, as it contributes to pathological incidence and clinical mortality. For example, the SASP promotes several hallmarks of cancer, while the elimination of senescent cells delays tumorigenesis [6]. The number of senescent cells tends to increase with age in almost all mammalian species, resulting in remarkably shortened healthspan and compromised lifespan [7, 8].

Single-cell profiling at both transcriptomic and proteomic levels suggests that senescent cells undergo intense metabolic reprogramming in order to maintain their cycle-arrested but viable status, and upregulate the expression of proteins essential to sustain the highly complex, dynamic and heterogeneous SASP [3, 9]. In fact, several forms of metabolic stresses can both drive senescence and trigger the SASP. Many drivers of mitochondrial dysfunction contribute to cellular senescence, through disruption of cytosolic nicotinamide adenine dinucleotide (NAD^+ and NADH), production of reactive oxygen species (ROS) and potentially other mechanisms. Specifically, the mitochondrial dysfunction-associated senescence (MiDAS) phenotype lacks some pro-inflammatory components of the SASP, including those associated with the interleukin 1 (IL-1)-dependent inflammatory arm, but these cells instead exhibit a distinct set of SASP factors [10]. MiDAS is primarily driven by the accumulation of cytosolic NADH, which is oxidized by mitochondria to NAD^+,

causing a reduced NAD^+/NADH ratio in cytosol and preventing the IL-1-associated SASP *via* AMPK-mediated p53 activation. Although the MiDAS phenotype appears to be independent of ROS and DNA damage, decrease of the NAD^+/NADH ratio inhibits the key glycolytic enzyme GAPDH, resulting in ATP depletion, AMPK activation and cell cycle arrest [10].

Senescent cells upregulate the protein level of the nicotinamide (NAM) salvage enzyme, namely nicotinamide phosphoribosyltransferase (NAMPT), while expression of the SASP markedly depends on NAD^+ availability [11]. Treating senescent cells with nicotinamide mononucleotide (NMN) can enhance the SASP, causing increased chronic inflammation and promoting development of inflammation-driven malignancies [12]. Thus, administration with NAD^+-boosting supplements, such as nicotinamide riboside (NR) and NMN, may come at the cost of systemic side effects, such as enhancing chronic inflammation and cancer incidence. As a substrate to a group of diverse enzymes, including poly(ADP-ribose) polymerases (PARPs) and sirtuins, NAD^+ is a critical nucleotide involved in oxidation-reduction reactions [13]. However, NAD^+ levels decrease during organismal aging and upon progeroid, causing metabolic dysfunction and a decline in physical fitness [14, 15]. Recent studies further suggested that NAD+ declines with age in a number of senescent cell-residing and metabolically active tissues in a $CD38^+$ macrophage-dependent manner, causally linking NAD exhaustion to both senescence and aging [16]. Despite these advances, a wide landscape of metabolic activities especially those correlated with glucose consumption and energy production, aspects essential to support the distinct protein synthesis machinery in senescent cells, as well as underlying central mechanisms, is largely lacking.

In this study, we aimed to characterize the senescence-associated metabolism and uncovered that that pyruvate dehydrogenase kinase isoform 4 (PDK4), a pyruvate dehydrogenase (PDH) inhibitory kinase playing a key role in the control of metabolic flexibility of glucose, is significantly upregulated in senescent cells. Although displaying a reduced NAD^+/NADH ratio, senescent cells maintain a hypercatabolic activity and produce an increased amount of pyruvate and lactate, metabolites correlated with elevated glycolysis.

PDK4 upregulation in stromal cells results in elevated aggressiveness of cancer cells, while targeting PDK4 restrains the impact of senescent cells on cancer cell malignancy, promotes tumor regression *in vivo* and extends posttreatment survival of animals. We further unmasked the implication of lactate in promoting NOX1-dependent ROS production, a process that exacerbates DNA damage and supports the SASP development. In advanced stage, pharmacologically suppressing PDK4 activity reduces physical dysfunction and alleviates frailty, improving late life health conditions. Together, there is an inherent link between cellular senescence, PDK4 upregulation, lactate production and age-related systemic degeneration, which may culminate in chronic disease development such as cancer progression. We propose a senescence-specific metabolic axis involving PDK4, a molecule that functionally underlies metabolic reprogramming and may be exploited therapeutically to counteract aging and age-related pathologies.

Results

Cytotoxic stimuli particularly genotoxicity induce cellular senescence and PDK4 expression

Pyruvate enters the TCA cycle through PDH, while PDK molecules (PDK1-4) inhibit PDH activity and promotes the switch from mitochondrial oxidation to cytoplasmic glycolysis. PDK4 is located in the mitochondrial matrix and inhibits the PDH complex by phosphorylating its E1α subunit, thereby contributing to glucose metabolism regulation [17]. Although predominantly expressed in the muscle and affects the metabolic fate of glucose during exercise, PDK4 is often studied in various cancer types [18-20]. However, insights into PDK4 expression in normal tissue microenvironments and its inducibility in response to stressful insults remain limited. We recently noticed that the stromal cell line PSC27, which is of human prostate origin and comprising mainly fibroblasts but with a minor percentage of non-fibroblast cell lineages such as endothelial cells and smooth muscle cells, produces a large array of SASP factors upon exposure to cytotoxic insults specifically genotoxic chemotherapy or ionizing radiation [21, 22]. Interestingly, PDK4 emerged as one of the

upregulated factors, together with a list of typical SASP components, as previously revealed by our microarray profiling (Fig. 1a and Extended Data Fig. 1a) [21]. To confirm, we expanded by employing several alternative approaches to induce senescence, including replicative exhaustion (RS), overexpression of $p16^{INK4a}$ (p16) and $HRas^{G12V}$ (RAS), respectively. These treatments caused comprehensive cellular senescence, with an efficacy resembling that of DNA-damaging agents such as radiation (RAD), bleomycin (BLEO) and hydrogen peroxide (HP) (SA-β-Gal positivity and BrdU incorporation, Extended Data Fig. 1b-d). In each case, we observed a pronounced induction of PDK4 in senescent cells (Fig. 1b, c).

Expression analysis of several cell lines of human prostate origin suggested that stromal cells are indeed more PDK4-inducible than cancer epithelial cells, implying a special mechanism supporting PDK4 production in prostate stromal cells posttreatment (Fig. 1d). Data from several additional fibroblast lines consistently supported a robust induction of PDK4 upon treatment by genotoxic anticancer agents (Fig. 1e). Notably, the transcript expression pattern of PDK4 largely phenocopied that of a number of hallmark SASP factors including MMP1, WNT16B, SFRP2, SPINK1, MMP3, CXCL8, EREG, ANGPTL4 and AREG, which exhibited a gradual increment until cells entered a platform within 5-7 days after treatment (Fig. 1f, g). Among the family of human PDKs (PDK1-4 isozymes), PDK4 appeared to be the only member readily inducible by genotoxic stress, with a tendency similar to that of CXCL8, an index of the SASP expression (Fig. 1h, i).

PDK4 expression in stroma predicts adverse clinical outcomes post-chemotherapy

Experimental data derived from *in vitro* assays prompted us to further determine whether PDK4 induction occurs within the tumor microenvironment (TME), a pathological entity where a plenty of benign stromal cells reside. We first chose to analyze clinical samples of a cohort of prostate cancer (PCa) patients who developed primary tumors in the prostate and underwent neoadjuvant chemotherapeutic regimen involving genotoxic agents such as mitoxantrone (MIT). Surprisingly, PDK4 was found markedly expressed in prostate tissues of these patients after neoadjuvant chemotherapy, but not before (Extended Data Fig. 2a). Basically in line with our *in vitro* data, upregulated PDK4 was generally localized in the

stroma, in a sharp contrast to the adjacent cancer epithelium which had limited or no staining.

PDK4 production in patient samples pre- *vs* post-chemotherapy was quantitatively measured by a pre-established pathological assessment procedure, which allowed precise evaluation of the expression of a target protein *per* immunohistochemistry (IHC) staining intensity (Extended Data Fig. 2b). Transcript analysis upon laser capture microdissection (LCM) of cell lineages from primary tissues suggested that PDK4 was more readily induced in the stromal rather than cancer cell subpopulations ($P < 0.0001$ *vs* $P > 0.05$) (Extended Data Fig. 2c). To substantiate PDK4 inducibility *in vivo*, we profiled a subset of PCa patients whose pre- and post-chemotherapy biospecimens were both accessible, and found remarkably upregulated PDK4 in the stroma, but not cancer epithelium, of each individual post-chemotherapy (Extended Data Fig. 2d, e). We noticed the dynamics of PDK4 expression in the damaged TME largely in parallel to that of CXCL8 and WNT16B, two canonical SASP components (Extended Data Fig. 2f). Expression pattern of these factors were largely consistent with that of senescence markers including $p16^{INK4a}$ and $p21^{CIP1}$ in tumor foci, suggesting an inherent correlation of PDK4 induction with cellular senescence and the SASP (Extended Data Fig. 2f). Of note, Kaplan-Meier analysis of PCa patients stratified according to PDK4 expression in tumor stroma suggested a significant but negative correlation between PDK4 protein level and disease-free survival (DFS) in the treated cohort ($P < 0.05$, log-rank test) (Extended Data Fig. 2g).

The distinct pathological properties of PDK4 in PCa were subsequently reproduced by an extended study, which was designed to recruit clinical cohorts of human breast cancer (BCa) patients (Supplementary Fig. 1a-d). Implicating the functional roles of PDK4, such as working as a critical regulator of epithelial-to-mesenchymal transition (EMT) and drug resistance of human cancers [19], data from gene expression profiling interactive analysis (GEPIA) with the cancer genome atlas (TCGA) and genotype-tissue expression (GTEx) databases indicated that PDK4 expression in cancer cells *per se* is associated with the poor prognosis of some, but not all cancer types (Supplementary Fig. 1e-f). Thereby, in contrast to former studies that mainly focused on PDK4 expression in cancer cells *per se*, our data

consistently suggest that PDK4 induction in tumor stroma may act as an SASP-associated independent predictor of clinical prognosis, holding the potential to be exploited for stratifying the risk of disease relapse and clinical mortality of posttreatment patients. Given such a pathological relevance, it is reasonable to speculate that PDK4 production by the stroma may have a causal role in senescence-related conditions, such as cancer progression.

Senescent cells exhibit a distinct profile of glucose metabolism

A typical feature of cancer cells is the ability of reprogramming energy metabolism to fuel their expansion and survival, while enhanced mitochondrial function plays important roles in tumor development [23]. One of the major hallmarks of senescent cells is that they remain metabolically active and synthesize a plethora of protein factors (SASP) with the capacity to affect other cells of host microenvironment locally or systemically [24]. Former studies on the metabolism of cellular senescence demonstrated that levels of both glucose consumption and lactate production are elevated during senescence [25]. While increased expression of glucose transporter and glycolytic enzymes during cellular senescence was observed, to date relevant data were mostly derived from cancers such as lymphomas and melanomas, or senescent cells induced by activation of oncogenes (OIS) such as $BRAF^{V600E}$, with metabolic signaling axis partially elucidated in senescent cancer cells [26, 27]. In contrast, the metabolic feature of glucose, a major energy source of senescent cells, especially those of stromal origin and non-cancerous entity, as well as the influence of such a metabolic profile on surrounding tissue homeostasis, remain generally unclear and merits in-depth understanding.

Glucose is the primary carbon source to the tricarboxylic acid (TCA) cycle, followed by glutamate and aspartate (non-protonatable amino acids as glutamine or asparagine, respectively) as secondary sources (Fig. 2a) [28]. We first interrogated the metabolic pattern of glucose upon uptake by senescent cells, as glucose is supposed to act as a principal contributor to the TCA cycle when cells enter senescence, a stage that allows cells to sustain metabolic activity [29]. Experimental data from analysis of mitochondrial dynamics and cellular bioenergetics with the gas chromatography-mass spectrometry (GC-MS) indicated significantly elevated glycolytic activity in senescent human stromal cells, as reflected by

enhanced production of metabolites including but not limited to dihydroxyacetone phosphate (DHAP), glyceraldehyde-3-phosphate (GAP) and 3-phosphoglycerate (3-PG) (Fig. 2b). Increased levels of GAP and 3-PG imply further utilization of a number of middle metabolites, such as citrate, α-ketoglutarate, glutamate, succinate, fumarate and malate in TCA cycle, metabolically derived from pyruvate, which was indeed substantiated by results from metabolic profiling with GC-MS (Fig. 2c and Extended Data Fig. 3a-g). Together, bioactivities of both glycolysis and TCA cycle were significantly enhanced in senescent cells, as reflected by an overall profiling with assays of stable isotope labelling with a uniformly labelled U-$^{13}C_6$ glucose tracer and fractioning of metabolites derived from labelled glucose and revealed by GC-MS (Fig. 2d). Of note, entry of glucose-derived and PDH-catalyzed flow of carbon into the TCA cycle generates isotopomer species with two labeled carbons (M2), while species with more labeled carbons (M3 and M4) arise from addition of labeled acetyl-CoA to labeled oxaloacetate produced by TCA cycling (Fig. 2a) [30]. As compared with their proliferating counterparts, senescent cells seem to display an increased rather than decreased citrate M2/pyruvate M3 ratio, further implying an enhanced TCA cycle activity alongside the simultaneously increased glycolytic capacity (Extended Data Fig. 3h), a feature that makes them remarkably distinct from most types of cancer cells.

Further, we noticed that these metabolic changes were accompanied by substantial perturbations in mitochondrial ultrastructure of senescent cells, particularly enlarged sizes and abnormal shapes as revealed by transmission electron microscopy (TEM), a phenomenon indicative of ultrastructural damage of mitochondria and suggesting potential mitochondrial dysfunction associated with oxidative stress upon cellular senescence (Fig. 2e). These observations are largely consistent with former studies regarding abnormal phenotypes of mitochondria including their mass, dynamics and structure in senescent cells [31].

We next measured the levels of extracellular fluids. Strikingly, the amounts of both pyruvate and lactate released to the extracellular space were considerably enhanced in senescent cells relative to their proliferating counterparts (Fig. 2f). These changes were accompanied by alterations in oxygen consumption rate (OCR) and extracellular

acidification rate (ECAR) as determined by the XF24 Extracellular Flux analyzer (Seahorse Bioanalyzer), suggesting elevated metabolic activities associated with glucose utilization (Fig. 2g and Extended Data Fig. 3i-k). Correspondingly, we observed elevated ATP production, basal respiration, maximum respiration in senescent cells, a pattern indicative of tight connection of TCA cycle and oxidative phosphorylation (OXPHOS) but further promoted when PDK4-IN-1, an anthraquinone derivative and a potent inhibitor of PDK4 (referred to as PDK-IN hereafter) [32], was applied to culture (Fig. 2h-j). However, treatment with PDK4-IN reversed changes in non-mitochondrial oxygen consumption, pH fluctuation, lactate production and H^+ (proton) leak, with the overall metabolic data validated by principal component analysis (PCA) scores (PC1 *vs* PC2) (Fig. 2k-n and Extended Data Fig. 3l). There alterations occurred in parallel with expression changes of glucose uptake-associated molecules and metabolism-related enzymes including glucose transporter 1 (GLUT1), hexokinase 2 (HK2), lactate dehydrogenase A (LDHA), isocitrate dehydrogenase 2 (IDH2), isocitrate dehydrogenase 3 (IDH3), oxoglutarate dehydrogenase (OGDH) and citrate synthase (CS) (Extended Data Fig. 3m). Among them, HK2 and LDHA are glycolysis-related factors, while IDH2, IDH3, OGDH and CS are TCA cycle-associated enzymes. As overexpression of PDK4 *per se* in normal cells neither caused or abrogated cellular senescence, nor affected the SASP (Extended Data Fig. 3n, o), we reasoned that the metabolic profile of senescent cells was correlated with and likely underpinned by expression of key factors involved in glucose consumption and linked with production of pyruvate, lactate and multiple other metabolites. Notably, elevated levels of glycolysis and oxidative phosphorylation were simultaneously observed, suggesting essentially reprogrammed glucose metabolism upon cellular senescence.

Former studies reported that in contrast to proliferating cells, senescent cells exhibit increased glucose transporter and glycolytic enzyme expression levels after chemotherapeutic treatment [26], a feature largely confirmed by our experimental data (Extended Data Fig. 3m). Steady state glucose concentrations tend to be higher in senescent cells as compared to their control, suggesting an elevated glucose avidity upon senescence. These findings are essentially confirmed by metabolomics profiling, which underscores the

global catabolic nature of senescence-associated metabolic alterations. Taken together, senescent cells develop a distinctive hypermetabolic phenotype characterized of enhanced glycolysis, TCA activity and ATP-boosting oxidative phosphorylation. Increased energy production is a common denominator of senescent cells, which exhibit a specific utilization of energy-generating metabolic pathways, a phenomenon partially reminiscent of the 'Warburg effect' typically observed in cancer cells capable of performing a non-oxidative breakdown of glucose [26].

Senescent cells consume glucose to produce lactate *via* expression of PDK4

Data from previous studies indicated that senescent cells are in a hypermetabolic status, more specifically, these cells display a hypercatabolic nature [26], thus prompting us to interrogate whether these cells have a glucose uptake capacity distinct from that of proliferating cells. To address this, we performed another set of metabolic assays. Not surprisingly, a significant increase of glucose uptake by senescent cells was observed, although with the alteration preferentially detected upon genotoxicity-induced senescence (GIS), which usually involves DNA-damaging agents (Fig. 3a). Further, the pH of conditioned media (CM) from senescent cells was markedly decreased, a property that again seemed to be more dramatic for senescence induced by genotoxic stress (Fig. 3b). Given the results indicative of an elevated acidification potential as revealed by the ECAR assay (Extended Data Fig. 3i), we reasonably speculated the extracellular formation of an acidic microenvironment by senescent cells, whose metabolism appeared to be distinctly reprogrammed and was characterized with increased secretion of acidic metabolites. Our data suggested that senescent cells can generate an increased amount of lactate, which was higher than their cycling control counterparts (Extended Data Fig. 4a). Multiple studies reported that cancer cells have increased lactate production, OCR level and ATP production, a series of metabolic changes correlated with enhanced glycolysis [33, 34]. Strikingly, we found that many relevant activities of senescent cells were even higher than those of cancer cells selected as of the same organ origin (herein, prostate), such as PC3 and DU145, although with several key features manifesting changes evidently opposite to those of examined cancer lines (Extended

Data Fig. 4a-f).

PDK4 is a key enzyme involved in the regulation of glucose and fatty acid metabolism as well as tissue homeostasis, while its overexpression inactivates the PDH complex by phosphorylating the targets and contributes to metabolic flexibility. We assessed the influence of PDK4 expression by transducing a PDK4 construct to human stromal cells, and noticed significantly altered metabolic profile including glucose uptake, lactate production and triglyceride (TG) production, although these changes were largely reversed upon genetic eliminated of PDK4 (Extended Data Fig. 4g-i). Of note, a decreased pH of the CM was observed in the case of PDK4 overexpression in proliferating cells, but subject to counteraction by PDK4 suppression (Extended Data Fig. 4j). We further measured these parameters with senescent cells induced by BLEO treatment, and found markedly increased glucose uptake, lactate production and TG production, but reduced pH of the CM (Extended Data Fig. 4k-n). However, almost all these metabolic changes were substantially reversed, when PDK4 was depleted from PSC27, except the TG levels, a case suggesting a PDK4-mediated antagonism against TG synthesis throughout the TCA cycle in senescent cells (Extended Data Fig. 4k-n). We noticed that factors functionally supporting glycolysis and TCA, including GLUT1, MCT4, HIF1α, PGK1, PGI, CS, IDH2, IDH3A and IDH3B were concurrently upregulated upon GIS, further indicating an overall enhancement of cell metabolism with the glucose as an energy source (Extended Data Fig. 4o).

NAD^+ and its reduced form, NADH, are pivotal coenzymes for redox reactions and play critical roles in energy metabolism [35]. The intracellular level of NAD^+ is frequently altered during aging and upon age-related pathologies. We previously generated SoNar, an intensely fluorescent, rapidly responsive, pH-resistant and genetically encoded sensor for tracking subtle changes in cytosolic NAD^+ and NADH redox states by imaging and quantifying the NAD^+/NADH ratio in living cells and *in vivo* [36], but the metabolic profile NAD^+ and NADH in senescent cells remains largely undefined (Fig. 3c). We first measured the intracellular NAD^+/NADH redox state of PSC27 cells utilizing SoNar's fluorescence (Fig. 3d-f). The data indicated a remarkably lower NAD^+/NADH ratio upon TIS (evidenced by increased

NADH/NAD^+), a pattern that was essentially subject to reversal by the PDK4 inhibitor, suggesting a remarkably elevated reduction of NAD^+ to NADH, a process accompanied by enhanced glycolysis (Fig. 3g, h). As another technical advancement, we designed FiLa, a highly responsive, ratiometric and genetically encoded lactate sensor to monitor the production and consumption of lactate at subcellular resolution [37] (Fig. 3i, j). We observed a remarkable increase in cytosolic lactate upon cellular senescence, albeit essentially abrogated in the case of PDK4 functional deficiency (Fig. 3k, l). The results from fluorescence sensors suggest that the lactate production level increases in parallel to the NAD^+/NADH ratio decrease in senescent cells, while both changes are correlated with PDK4 activity. The data not only disclose the concurrent fluctuation of NAD^+/NADH conversion and lactate generation, but further substantiate the central role of PDK4 in orchestrating a metabolic profile specifically associated with the occurrence of cellular senescence.

$PDK4^+$ stromal cells alter the expression profile and phenotypes of cancer cells *via* HTR2B

We next sought to determine the influence of stromal cells expressing PDK4 on their surrounding microenvironment, specifically cancer cells. Since PSC27 originally derived from human prostate, we first chose to examine PCa cells. PSC27-derived CM was prepared to treat PCa cells in culture, with cancer cells subject to genome-wide analysis. Data from RNA sequencing (RNA-seq) indicated that 4188 transcripts were significantly upregulated or downregulated (fold change > 2, $P < 0.05$) in PC3 cells, with 4860 and 3756 transcripts changed in DU145 and M12 cells, respectively (Fig. 4a). We noticed remarkable and comprehensive changes in the biological processes of PCa cells, as evidenced by considerably affected activities in signal transduction, cell communication, intracellular transport, energy pathways and metabolism regulation (Fig. 4b and Extended Data Fig. 5a, b). Together, the data suggest a salient capacity of PDK4-expressing stromal cells in reprogramming the transcriptome of recipient cancer cells through production of the CM.

Among the transcripts significantly upregulated by the CM of PSC27 cells ($P < 0.05$,

FDR < 0.01, top 1000 shown *per* PCa line, Supplementary Table 1), we noticed that there were 7 transcripts showing up and commonly expressed by PC3, DU145 and M12 cells (fold change > 4, $P < 0.01$) (Fig. 4c, d). We then chose to focus on a specific gene (or more accurately, transcript), which potentially contributes to malignant progression of cancer cells. Immunoblots substantiated that expression of 5-hydroxytryptamine receptor 2B (HTR2B), a gene encoding one of the several different receptors for serotonin which belongs to the G-protein coupled receptor 1 family and plays key roles in a few essential activities[38], was markedly induced upon exposure of PCa cells to the CM of PDK4-expressing stromal cells (Fig. 4e). Serotonin is a biogenic hormone that functions as a neurotransmitter and a mitogen, while serotonin receptors mediate the central and peripheral physiologic functions of serotonin, including regulation of cardiovascular functions and impulsive behavior. We interrogated the implications of HTR2B in phenotypic changes of individual PCa cell lines. The capacities of proliferation, migration and invasion of PCa cells were comprehensively enhanced, as evidenced by our *in vitro* assays (Fig. 4f-h). More importantly, transduction of HTR2B enhanced the resistance of PCa cells to MIT, a DNA-targeting chemotherapeutic agent administered to cancer patients including those developing PCa [39, 40] (Fig. 4i). The survival curves of cancer cells under genotoxic stress of MIT displayed a shift toward higher concentrations of this drug, as exemplified by the case of PC3 (Fig. 4j). The CM derived from senescent stromal cells generated by BLEO treatment (PSC27 (BLEO) CM) caused a more dramatic increase of chemoresistance than HTR2B *per se*, suggesting the presence and contribution of other molecules in the CM of senescent stromal cells, particularly a large number of soluble factors encoded by the full-spectrum of the SASP. However, these gain of functions were generally lost when LY 266097 [41], a selective antagonist of HTR2B, was applied to the culture, suggesting that enhanced malignancies of cancer cells can be mainly attributed to the activity of HTR2B after ectopically expressed in these lines (Fig. 4f-j).

As HTR2B is one of the most upregulated genes observed in PCa lines we examined upon treatment with PDK4$^+$ stromal cell CM, whether or not it accounts for the principal force driving malignant changes of recipient cancer cells remain unknown. We then used LY 266097 or gene-specific small hairpin RNAs (shRNAs) to target HTR2B in individual PCa

cell lines before performing phenotypic assays. Interesting, the gain of functions conferred by the CM of PDK4$^+$ stromal cells was substantially abrogated in the absence of HTR2B or upon LY 266097 treatment (Extended Data Fig. 5c-g). Thus, HTR2B is a competent factor that mediates the influence of the lactate-enriched microenvironment generated by PDK4-expressing stromal cells on recipient cancer cells, while elimination of HTR2B or blockade of HTR2B signaling in cancer cells holds the potential to remarkably weaken their malignant phenotypes.

As an energy source, glucose is converted to pyruvate, the latter then partially reduced to lactate *via* LDH and excreted from senescent cells. Since export of lactate into the microenvironment maintains intracellular pH and recycles NADH, both essential for sustaining metabolic activities, we queried human cancer cell-associated uptake pattern and utilization profile of exogenous lactate, one of the major glycolytic by-products released by senescent cells and holding the potential to be employed for investigating the flux of metabolites once specifically labeled. To this end, we chose to supply with L-[1-^{13}C] lactate (10 mM) in culture, a condition that largely mimicks the concentration of lactate produced by senescent stromal cells and allows tracing and fractioning of metabolites of recipient cells. The input of L-[1-^{13}C] lactate in culture led to intracellular enrichment of exogenous lactate in both PC3 and MDA-MB-231 cells (higher than 5.0%) (Extended Data Fig. 6a, b). The presence of ^{13}C-enriched pyruvate and alanine was observed, albeit the latter exhibiting an even higher fraction, suggesting a conversion of ^{13}C-labelled lactate and subsequent intracellular flow in these cells. In contrast to the citrate fraction, there seems to be less accumulation of other ^{13}C-enriched TCA intermediates as well as derivatives, including but not limited to α-KG, glutamine, succinate and fumarate, indicating the mitochondrial turnover of ^{13}C-carbons through a regular TCA cycling (Extended Data Fig. 6c).

Monocarboxylate transporters (MCTs) play a major role in intercellular lactate/H$^+$ traffick and pH homeostasis regulation. Among diverse MCT isoforms, MCT1 and MCT4, are found to be essential in maintaining an appropriate environmental acidity through lactate transport, with their high expression associated with cancer aggressiveness and poor

prognosis [42]. We noticed elevated levels of MCT1 (PC3) and MCT4 (MDA-MB-231) upon exposure of cells to exogenous lactate, implying upregulation of these MCTs in response to lactate addition (Extended Data Fig. 6d, e). Importantly, treatment with syrosingopine, a dual inhibitor of MCT1 and MCT4 [43], caused a significant decrease (> 50%) of each of the fore-mentioned metabolites (Extended Data Fig. 6a, b), supporting the critical role of MCT1 or MCT4 in mediating the transport of exogenous lactate, a metabolic product that can be substantially produced by senescent stromal cells in the microenvironment.

Therapeutically targeting PDK4 improves chemotherapeutic outcome in preclinical trials

Given the lactate-enriched extracellular microenvironment formed by stromal cells expressing PDK4 and its effects on the biological phenotype and expression profile of cancer cells *in vitro*, we were tempted to query the pathological consequences of PDK4 induction in the TME under *in vivo* conditions. To this end, we constructed tissue recombinants by admixing PSC27 sublines with PC3 cells at a pre-optimized ratio of 1:4 before subcutaneous implantation to the hind flank of experimental mice with severe combined immunodeficiency (SCID). The animals were gauged for tumor size at the end of an 8-week period. Compared with tumors comprising PC3 and $PSC27^{Vector}$, xenografts composed of PC3 and $PSC27^{PDK4}$ displayed significantly increased sizes ($P < 0.01$) (Extended Data Fig. 7a). Conversely, PDK4 knockdown by shRNA from these $PSC27^{PDK4}$ cells prior to xenograft implantation markedly reduced tumor volumes ($P < 0.01$ and $P < 0.05$, respectively).

To closely mimic clinical conditions involving chemotherapeutic agents, we designed a preclinical regimen incorporating a genotoxic drug (MIT) and/or the PDK4 inhibitor (PDK4-IN) (Fig. 5a). Two weeks after cell implantation when stable uptake of tumors by host animals was generally observed, a single dose of MIT or placebo was administered at the 1st day of 3rd, 5th and 7th week until the end of the 8-week regimen (Extended Data Fig. 7b). Although PDK4-IN administration did not provide noticeable benefits, MIT treatment caused remarkable tumor shrinkage (57.5% volume reduction), validating the efficacy of

MIT as a cytotoxic agent (Fig. 5b). Importantly, when PDK4-IN was combined with MIT, a further decline of tumor volume was observed (35.5%), resulting a total shrinkage by 72.6% as compared with the vehicle control.

Not surprisingly, we observed a considerable upregulation of typical SASP factors such as IL6, CXCL8, MMP3, SPINK1 and AREG, accompanied by expression of typical senescence markers including $p16^{INK4a}$ and $p21^{CIP1}$ in stromal cells of xenografts composed of PC3/PSC27 cells, implying development of *in vivo* senescence and expression of the SASP upon MIT treatment (Fig. 5c and Extended Data Fig. 7c, with the group of the lowest value used as the normalization baseline *per* factor). Although PDK4-IN alone neither induced nor affected cellular senescence, it restrained expression of these hallmark SASP factors in the MIT-treated group (Fig. 5c and Extended Data Fig. 7c). Although senescence was induced in cancer cells in animals undergoing MIT treatment as suggested by $p16^{INK4a}$ and $p21^{CIP1}$ expression, we did not observe a typical and full-spectrum SASP in these cells, which were of epithelial origin in nature, results largely consistent with our former findings [44, 45]. Of note, PDK4 expression was remarkably induced in stromal cell populations, but not in their epithelial counterparts (Extended Data Fig. 7c), basically in line with our *in vitro* data (Fig. 1d, e). Histological staining indicated elevated SA-β-Gal positivity in tumor tissues of mice that experienced MIT treatment, but exposure to PDK4-IN resulted in a relatively lower SA-β-Gal positivity, suggesting that PDK4 likely contributes to cellular senescence in animals undergoing chemotherapy (Fig. 5d, e). These data indicate the operation of a mechanism allowing PDK4 to promote senescence, although this agent presumably neither targets DNA nor damages other macromolecules.

Given the primary *in vivo* expression results derived from treatments involving MIT and/or PDK4-IN, we next asked how pharmacologically targeting PDK4 could enhance the therapeutic response of tumors. To disclose the possible mechanism(s), we chose to dissect tumors from animals 7 days after initiation of treatment, a timepoint right prior to the development of resistant colonies. In contrast to vehicle, MIT *per se* caused significant DNA damage and apoptosis in cancer cells (Fig. 5f). Although PDK4-IN alone neither

caused typical DDR nor induced cell apoptosis, it showed prominent efficacy in enhancing these therapeutic indices upon combination with MIT ($P < 0.05$). IHC staining disclosed increased caspase 3 cleavage, a canonical apoptosis indicator, upon MIT administration, with the tendency further enhanced by PDK4-IN (Fig. 5g).

To expand, we used LNCaP, a second PCa cell line which expresses androgen receptor (AR) and is routinely employed as a hormone-responsive cell model. To produce an AR-naïve setting, we circumvented experimental castration, but followed the same protocol designed for PC3-tailored therapeutic cohorts. We noticed significantly reduced volumes of LNCaP/PSC27 tumors when mice underwent MIT/PDK4-IN co-treatment, in contrast to MIT administration only (36.1%) (Extended Data Fig. 7d). Similar results were observed when 22Rv1, a castration-resistant PCa cell line, was applied to replace LNCaP for *in vivo* assays (35.3%) (Extended Data Fig. 7e). As supporting efforts to exclude the possibility of tumor type specificity, we generated xenografts composed of MDA-MB-231 and HBF1203, the latter a breast stromal cell line. The results largely produced those observed in animals carrying PCa tumors (39.8%) (Extended Data Fig. 7f). Together, these data suggest that specific targeting of PDK4, a kinase responsible for lactate production upon glucose metabolism, specifically in a treatment-damaged TME which harbors a considerable number of senescent cells, can substantially promote tumor regression in chemotherapeutic settings, a process independent of androgen regulation or AR signaling of prostate tumors *per se*. We hereby conclude that the resistance-minimizing effects of PDK4-targeting strategy are not limited to a specific cancer type, but may have implications to a wide range of malignancies.

We next assessed tumor progression consequence by comparing the survival of different animal groups in a time-extended preclinical cohort, with PCa mice as a pilot model. In the course of tumor growth surveillance, a bulky disease was considered developing once the tumor burden was prominent (size $\geq$ 2000 mm^3), an approach described previously [22, 46]. Mice that received MIT/PDK4-IN combinational treatment displayed the most prolonged median survival, gaining a 40.9% longer survival when

compared with those treated by MIT only (Fig. 5h, green *vs* blue). However, PDK4-IN treatment alone did not achieve significant benefits, as it conferred only marginal survival advantage (Fig. 5h, brown *vs* red). Thus, targeting PDK4 alone in the TME affects neither tumor growth nor animal survival, while MIT/PDK4-IN co-treatment has the competence to significantly improve both parameters.

Importantly, to establish the safety and feasibility of such therapeutic regimens, we conducted routine pathophysiological appraisal. The data supported that either single or combinatorial treatment was well tolerated, as evidenced by body weight maintenance throughout the therapeutic timeframe (Supplementary Fig. 2a). Further, there were no significant perturbations in the serum level of creatinine, urea and metabolic activities of liver enzymes (ALP and ALT) (Supplementary Fig. 2b). Additional data from mice developing NSCLC carcinomas and treated by DOX(doxorubicin)/PDK4-IN generally phenocopied PCa animals (Supplementary Fig. 2c, d). Besides organ function integrity as indicated by basic biochemical indices, *in vivo* safety was further demonstrated by MIT/PDK4-IN-treated and DOX/PDK4-IN-treated immunocompetent animals (C57BL/6J background) which manifested no routine blood count fluctuations, thus essentially validating the feasibility of these therapeutic regimens (Supplementary Fig. 3a-f). Our data support that strategies combining a PDK4-targeting agent with classical chemotherapy hold the potential to enhance tumor responses without causing severe systemic cytotoxicity.

TIS-associated serum lactate adversely predicts posttreatment survival of cancer patients

Although higher PDK4 expression in the tumor foci is correlated with lower survival of posttreatment in clinic settings (Extended Data Fig. 2g and Supplementary Fig. 1d), whether the metabolite lactate derived from the TME harboring stromal cells that develop TIS is technically detectable and whether it can serve as a marker for clinic purposes, remains largely unknown. To address this, we acquired peripheral blood samples from PCa patients, including one cohort that experienced standard neoadjuvant chemotherapy and the other that did not. ELISA assays of the serum from chemo-treated patients revealed that

lactate levels in the treated cohort were significantly higher than that of the treatment-naïve group (Fig. 6a). The pattern was essentially reproduced by a remarkable increase of CXCL8 and SPINK1, canonical hallmarks of the SASP, in the same cohort of posttreatment patients (Fig. 6b, c). The data suggest that a circulating scale of lactate, the product of glucose metabolism *via* the glycolysis branch, emerges in the peripheral blood alongside with an *in vivo* SASP, which is intimately correlated with *in situ* senescence of tissues and develops after chemotherapeutic regimens, and both are systemically traceable in the serum of cancer patients. It is intriguing to determine whether the blood level of lactate is correlated with that of typical SASP factors such as CXCL8 and SPINK1 in the same individual patients after clinical treatment. Subsequent analysis of ELISA data disclosed a significant and positive correlation between lactate and CXCL8, as well as between lactate and SPINK1 (Fig. 6d, e). Thus, lactate production and SASP expression is mutually linked, largely resembling the correlation between PDK4 induction and the SASP factors as revealed by our clinical data derived from tumor samples *per se* (Extended Data Fig. 2f).

We then expanded the study by longitudinal analysis of these factors in both primary tumor foci and peripheral blood (20 chemo-treated patients randomly selected). Surprisingly, cross-organ comparisons indicated a pronounced association between in-tissue expression and circulating level *per* factor, with the amounts of lactate, CXCL8 and SPINK1 apparently varying in parallel either within the primary tissue or through peripheral blood of each individual (Fig. 6f). Together, our data suggests that lactate represents one of the critical TME-derived biological factors precisely imaging the development of an *in vivo* SASP, and can be exploited to assess the SASP magnitude in posttreatment cancer patients.

Clinical profiling subsequently uncovered a negative correlation between plasma level of lactate and posttreatment survival of PCa patients, further substantiating the pathological impact of lactate, which as a TME-derived molecule directly predicts adverse outcome once the TME is subject to irreparable damage by clinical agents (Fig. 6g). As PDK4 is subject to frequent mutation, amplification and deep deletion as disclosed by the TCGA

pan-cancer atlas studies (Querying 22179 patients/22802 samples in 36 clinical studies) which document global genomics data from multiple cancer types [47, 48] (Fig. 6h), this molecule represents an important predictor of disease progression in treatment-naïve patients in clinical oncology [49, 50]. Contrasting former studies which mainly focused on the genomic alterations and pathological behaviors of cancer cells, we herein propose that routine surveillance of lactate, a major metabolic product derived from enhanced glycolysis driven by PDK4 highly expressed in stromal cells particularly those in the case of TIS, *via* a noninvasive avenue such as liquid biopsy, can provide a novel, practical and accurate strategy for both prognosis and prevention of advanced pathologies in clinical oncology.

Lactate activates production of ROS *via* NOX1 induction in recipient senescent but not normal cells

Our data suggest that suppression of PDK4 activity partially affects senescence and the SASP (Fig. 5c-e, Extended Data Fig. 7c), whereas the underlying mechanism remains largely unclear. In the tissue microenvironment, lactate is usually a small molecule utilized as an energy source by cells, whereas it may also play other essential roles. We next queried whether and how the elevated production of lactate, which can result from PDK4 upregulation in senescent cells, affect their neighboring noncancerous counterparts. Lactate triggers ROS generation in mammalian cells *via* a mechanism involving the oxidation of lactate to pyruvate by lactate dehydrogenase (LDH), a process accompanied by the transformation of NAD^+ to NADH, while the latter can be further used by the NADPH oxidase (NOX) to generate ROS (Fig. 7a) [51, 52]. NOX is a superoxide $O_2(-)$-generating enzyme first identified in phagocytes showing bactericidal activities [53], and it remains intriguing to validate the lactate-NOX-ROS axis in our stromal cell-based system mainly composed of fibroblasts. Experimental data suggest that treatment of normal stromal cells (PSC27) with lactate at an experimentally pre-optimized concentration (10 mM) failed to induce ROS elevation (Fig. 7b). However, lactate exposure of cells developing mitochondrial deficiency, which was caused by treatment with chemicals such as rotenone and carbonyl cyanide m-chlorophenylhydrazone (CCCP) (an electron transport chain

complex I inhibitor and an OXPHOS uncoupler, respectively), resulted in substantially further elevated ROS production, as evidenced by increased signals of 2',7'-dichlorofluorescein (DCF), the latter derived from the fluorogenic probe 2',7'-Dichlorodihydrofluorescein-diacetate ($DCFH_2$-DA) (Fig. 7b).

NOX family is composed of five homologs, NOX1 to NOX5, and two related enzymes, DUOX1 and DUOX2. We observed enhanced expression of NADPH oxidase 1 (NOX1), but not other homologs of the NOX family, after lactate treatment of senescent, but not proliferating PSC27 cells (Fig. 7c and supplementary Fig. 4a). APX-115, a pan-NOX inhibitor, markedly reduced the expression of NOX1, but not other NOX molecules. To consolidate, we assessed potential treatment-caused effects on lactate production upon exposure of stromal cells to PDK4-IN, an experimental assay that allowed to examine the ROS biogenesis mechanism from the opposite side. Inhibition of PDK4 activity markedly diminished the capacity of genotoxicity-induced senescent cells in producing the ROS, a tendency largely reproduced by treatment with ML-090 or APX-115, the former a chemical inhibitor against NOX1 (Fig. 7d). As DDR events are typically responsible for the ROS generation in senescent cells, we questioned the possibility of lactate in promoting genotoxicity *via* ROS production. Immunofluorescence staining suggested substantially reduced intensity of DDR foci in BLEO-damaged cells upon exposure to PDK4-IN, although the agent did not cause changes to proliferation cells (Fig. 7e, f). Of note, expression of CXCL8, one of the hallmark factors of the SASP, exhibited reduced expression upon PDK4 suppression, a pattern largely consistent with the vast majority of other SASP factors (Fig. 7g, h and Extended Data Fig. 8a). In contrast to signal intensities of NOX1 induction and DDR activation, the latter imaged by phosphorylated H2AX (γH2AX), expression of p16 and PDK4 seemed largely unaffected by PDK4-IN, suggesting differential regulatory mechanisms that modulate the expression or activation of these molecules (Fig. 7g). Transcriptome-wide profiling by RNA-seq indicated the presence of a large array of genes whose expression was significantly upregulated upon exposure to BLEO-delivered genotoxicity, a tendency substantially altered in the presence of PDK4-IN (Fig. 7h). Among the genes whose induction seems to be reversed upon PDK4

suppression, many indeed encode secreted factors falling in the SASP spectrum. Therefore, PDK4 induction-associated lactate production is responsible for activation of NOX1, which potently drives the generation of ROS and contributes to the SASP development, a process accompanied by the elevated DDR signaling, while inhibiting PDK4 activity or lactate-production pathway holds the potential to restrain senescence-associated phenotypes, particularly the SASP.

Cell damage can be triggered by multiple stressors, resulting in development of senescence in the form of either RS, OIS or TIS. To experimentally substantiate findings correlated with the implication of lactate, specifically upon production by senescent cells *via* the autocrine manner, in cell phenotypic development, we chose to examine the effect of PDK4 suppression in settings of replicative exhaustion (RS), oncogenic $HRas^{G12V}$ expression (OIS) and an alternative chemotherapeutic agent DOX (TIS). Cell-based assays demonstrated that the ROS production capacity of senescent cells was generally minimized by PDK4-IN (Extended Data Fig. 8b, c), a mitochondria-associated activity that was largely consistent with the alleviated DNA damage intensity of cells in each of these senescence-induction conditions (Extended Data Fig. 8d-f). We noticed remarkably reduced expression of typical SASP factors in these senescent cells, results basically reproducing those from assays performed upon cellular senescence induced by BLEO treatment (Extended Data Fig. 8g-i). In fact, once released into the extracellular space, lactate is freely accessible by recipient cells as either an autocrine or a paracrine metabolite, implying that senescent cells hold the potential to engage the ROS-SASP axis upon uptake of lactate, which can be derived from both types of sources in the microenvironment.

Targeting PDK4 at advanced stage alleviates physical dysfunction and extends lifespan of chronologically aged animals

Given the pharmacological development of a series of geroprotective agents targeting senescent cells particularly senolytics, which hold the potential to ameliorate various aging symptoms and improve age-related disorders, we queried whether administration of PDK4-specific agents such as PDK4-IN can postpone chronological aging and/or restrain age-

related phenotypes. To this end, we chose to treat normal 20-month-old wildtype (WT) mice with vehicle or PDK4-IN (20 mg/kg *via* i.p. injection) (once every 2 weeks) for 4 months, after which physical function (or fitness capacity) in these naturally aging animals was determined (Fig. 8a). Histological evaluation disclosed a significantly increased percentage of senescent cells within solid organs, as reflected by elevated SA-β-Gal-positivity in liver, lung, prostate and myocardial tissues of aged animals, changes that were partially but significantly reversed upon PDK4-IN treatment (Fig. 8b-f). However, the efficacy of PDK4-IN in minimizing the percentage of senescent cells in each tissue type seemed to be generally less remarkable than that of PCC1, a natural senolytic agent that can selectively eradicate senescent cell populations *in vivo* as we recently discovered [54].

Of note, age-dependent increase of alveolar volume, decrease of maximal speed, hanging endurance, beam balance performance, grip strength and motor skills, and reduction of daily activity were substantially improved in mice receiving administration of PDK4-IN in the old (20-month-old) mice compared with their counterparts experiencing vehicle treatment (Fig. 8g-m). Although the majority of the geroprotective effects generated by PDK4-IN seemed to be largely inferior to those caused by PCC1 intervention, we noticed the efficacy of these two agents still resembling each other in some cases. For instance, age-dependent expansion of pulmonary alveolus, a pathological change contributing to pulmonary dysfunction, was well controlled by both agents, as the therapeutic efficacy was similar between PDK4-IN and PCC1, although the latter holds a salient capacity of eliminating senescent cells from tissues (Fig. 8g). The data suggest a critical role of targeting PDK4 in restraining such an age-related pulmonary abnormality, as changes in the composition of the airways and the alveoli may result in reduced respiratory function and eventually lead to chronic lung disorders during mammalian aging. Importantly, we observed upregulation of NOX1 in multiple tissues of old animals, which was basically in line with elevated ROS levels *in vivo* (Extended Data Fig. 9a, b). Furthermore, expression of the SASP was considerable restrained in tissues such as the lungs (alveolar cells) of aged mice treated with PDK4-IN, as compared to those vehicle-treated animals (Extended Data Fig. 9c, d), a pattern consistent with reduced expression of

hallmark SASP factors by human stromal cells treated with PDK4-IN *in vitro* (Fig. 7j).

We then performed biochemical appraisal of the serum. Not surprisingly, the concentration of circulating lactate in serum was substantially reduced in old animals receiving PDK4-IN treatment, but without significant difference from those subject to PCC1 administration, implying the remarkable contribution of PDK4 in mediating lactate production in these mice (Fig. 8n). Cellular senescence plays a key role in the pathogenesis of nonalcoholic steatohepatitis (NASH) by promoting hepatic fat accumulation and steatosis in the course of aging [55, 56]. To dissect the potential of NASH development associated with natural aging and address the feasibility of controlling this pathology *via* targeting senescent cells, we examined a subgroup of mice at 20 months of age, and administered with vehicle, PDK4-IN or PCC1 for 4 months. In contrast to the young group, a number of old mice exhibited increased tendency to develop liver dysfunction, as indicated by elevated serum levels of alanine transaminase (ALT), aspartate transaminase (AST) and lactate dehydrogenase (LDH) (Extended Data Fig. 9e-g). However, administration of PDK4-IN significantly prevented these changes, suggesting PDK4 inhibition effectively ameliorated the pathogenesis of liver. Although PDK4-IN displayed efficacy in averting liver dysfunction, body weight and food intake levels remained largely unaffected in old mice (Extended Data Fig. 9h, i), suggesting the overall safety of such a PDK4-targeting regimen.

To establish the potential of limiting lactate production by senescent cells to prolong the remaining lifespan of very old animals, we performed PDK4 treatment beginning at an advanced stage (Fig. 8o). Mice receiving PDK4-IN administration (once every 2 weeks or biweekly) starting at 24-27 months of age (largely equivalent to an age of 75-90 years in humankind) had a 27.9% longer median post-treatment lifespan (or 4.0% longer overall lifespan) and lower mortality hazard (54.1%, $P < 0.001$) than the vehicle-treated group (Fig. 8p and Extended Data Fig. 9j). These data suggest that PDK4-specific intervention can significantly reduce the risk of age-related mortality in old mice.

As a minor but essential issue, we next sought to clarify whether the reduced mortality

in aged animals came at a cost of elevated late-life morbidity. To address this, we examined physical function of experimental mice exposed to vehicle, PDK4-IN or PCC1 (as a senolytic control *per* case) monthly until death. Despite the longer remaining lifespan in PDK4-IN-treated animals, physical function in the final 2 months of life appeared not significantly lower than that of vehicle-treated (Extended Data Fig. 9k-m). According to autopsy datasets, the cause of mortality, incidence of several age-related diseases and tumor burden were not remarkably different between animals treated by vehicle, PDK4-IN or PCC1 (Extended Data Fig. 10a-d). Nevertheless, expression of the SASP was reduced in solid organs such as the liver, a tendency largely consistent with the decline of circulating levels of interleukin 6 (IL6), amphiregulin (AREG) and colony-stimulating factor 3 (CSF3), typical SASP markers in the peripheral blood (Extended Data Fig. 10e-h).

Upon isolation of immune cells from the peripheral blood, we further observed reduced expression of the SASP in $CD3^+$ T cell subpopulations (Extended Data Fig. 10i), a cell lineage that displays robust upregulation of $p16^{INK4a}$ in the course of human ageing [57]. Of note, PDK4-IN minimized oxidative stress in liver tissues, as evidenced by a significant decrease of lipid peroxidation product 4-hydroxynonenal (HNE) adducts and a substantial increase in the ratio of reduced to oxidized glutathione (Extended Data Fig. 10j, k), data indicative of prominent benefits of PDK4 suppression in eliminating free radicals and engaging antioxidant defense system [58, 59].

Together, targeting PDK4, a member of the PDK protein kinase family contributing to the regulation of glucose metabolism, holds a remarkable potential to restrain the overall pathophysiological impact of senescent cells upon organismal aging, particularly systemic loss of tissue homeostasis and organ dysfunction resulting from lactate overproduced by these cells. As a technical advantage, regimens based on PDK4 suppression can significantly extend lifespan without causing elevated morbidity in animals. We hereby present proof-of-principle evidence that, even when administered in advanced stage, such a therapeutic strategy can remarkably postpone age-associated physical dysfunction, prevent age-related degeneration and optimize health conditions, thus establishing a

senescence-related and metabolism-oriented avenue to improve the healthspan and lifespan of aged individuals.

Discussion

Aging is defined as a complex and time-dependent process that causes a progressive decline of physiological integrity, particularly functional degeneration of multiple types of tissues and organs. A number of hallmarks contribute to aging, while cellular senescence is identified as one of the primary risk factors for the initiation and development of age-related conditions, such as cancers, diabetes, cardiovascular disorders and neurodegenerative diseases [4, 60]. Senescent cells synthesize a large array of pro-inflammatory cytokines, chemokines and extracellular matrix degrading enzymes, a feature known as the SASP [5]. Importantly, discovery of the SASP proposes a reasonable and critical mechanism to explain why senescent cells, even accumulating in a low number *in vivo* during aging, can generate large detrimental effects on organismal health. However, whether or not the SASP is the sole source of senescence-associated factors that contribute to the loss of tissue homeostasis and organ function, pathophysiological events directly linked with aging and age-related diseases, remains yet unknown. In this study, we mapped the metabolic landscape of glucose metabolism upon cellular senescence, and discovered that senescent cells develop a substantially reprogrammed metabolism and produce an increased amount of metabolites, particularly the glycolysis product lactate, the latter mediated by PDK4 upregulation and with the potential to alter the microenvironment. With experimental models, we demonstrated that consequences of such a metabolic rewiring include but are not limited to increased cancer malignancy, specifically enhanced drug resistance, and chronological aging accompanied by physical dysfunction in the advanced stage.

PDK4 plays a pleiotropic, dynamic and context-dependent role in regulation of glucose and fatty acid metabolism. Pyruvate enters the TCA cycle through PDH, the gatekeeping enzyme with its activity regulated *via* reversible phosphorylation for entry of pyruvate into TCA cycle by controlling the conversion of pyruvate into acetyl-CoA, while PDKs suppress PDH activity and promotes a switch from mitochondrial oxidation to cytoplasmic glycolysis

[50]. Belonging to the PDK superfamily and acting as a nutrient sensor and critical regulator of glucose homeostasis, PDK4 has become an attractive target for treatment of various metabolic pathologies including hyperglycemia, insulin resistance and hepatic steatosis [61]. Upregulation of PDK4 mediates aerobic glycolysis ('Warburg effect'), favors tumor growth and promotes apoptosis resistance [18, 62-64]. However, potential implications of PDK4 in senescence-associated phenotypes remain hitherto underexplored. Data of this study allowed us to establish PDK4 expression pattern upon cellular senescence, elucidate its role in diverging glucose metabolism towards glycolysis to produce lactate, and unravel the correlation of PDK4 upregulation in tumor stroma and patient survival post-chemotherapy. PDK4 expression is responsible for increased production of lactate, a molecule that accumulates in the treatment-damaged TME but ultimately enters the circulating system. Of clinical relevance, PDK4 expression in the TME is significantly and negatively correlated with disease-free survival of cancer patients in the posttreatment stage.

As previously demonstrated in an Eμ-myc transgenic mouse lymphoma model, TIS-competent and senescent lymphomas display increased glucose utilization and enhanced ATP production, features inherently linked to massive proteotoxic stress as a partial consequence of the SASP, while pharmacologically targeting these metabolic demands can prompt tumor regression and improve therapeutic outcomes [26]. These findings are largely consistent with our data and further validate the hypercatabolic nature of cells undergoing TIS, which is therapeutically exploitable by specific agents targeting key metabolic enzymes. Interestingly, $BRAF^{V600E}$-induced senescence, a form of OIS, exhibits downregulation of pyruvate dehydrogenase kinase1 (PDK1) and upregulation of pyruvate dehydrogenase phosphatase2 (PDP2), wherein the resultant activation of PDH enhances the use of pyruvate in TCA cycle and causes elevated respiration and redox stress [27]. Of note, Such a PDK1–PDP2–PDH axis was mainly observed in the case of OIS induced by $BRAF^{V600E}$, with the employed human diploid fibroblasts (HDFs) showing no changes in glucose uptake, despite alterations in OCR and secretion of pyruvate and glutamate [27]. More importantly, PDP2 and PDK1 are indeed crucially required for the metabolic wiring associated with, and the execution of, OIS, indicating that varying mechanisms can support development of metabolic profiles of different senescence types, a point that may trigger substantial interest

and deserves continued studies.

Senescent cells can be less efficient in ATP production, generating a bioenergetic imbalance with an increased AMP/ATP ratio, a fact that could be partially explained by a decreased efficiency of OXPHOS (characterized by less H^+ in the intermembrane space) associated with a reduction of mitochondrial membrane potential (MMP) [65]. Upon cellular senescence, however, we observed enhanced mitochondrial respiration, ATP production and increased oxidative stress as evidenced by elevated ROS, the latter may be due to mitochondrial dysfunction *per se*. These changes are presumably correlated with the enhanced uptake flux of glucose in senescent cells, which supports to meet the increased needs of energy and biosynthesis materials when the intracellular protein machinery is functionally engaged in synthesis of the full-spectrum SASP factors. TIS cells developing the SASP display endoplasmic reticulum stress, an unfolded protein response (UPR) and enhanced ubiquitination, while TIS cancer cells are more sensitive to glucose utilization blockade, a baseline for their selective elimination through pharmacological targeting of the metabolic demands [26]. Given our findings that unmask the hypercatabolic nature of senescent cells such as those undergoing TIS, it is reasonable to speculate the potential of therapeutically targeting metabolic features of these cells, a new modality of senotherapy exploitable to intervene aging and age-related conditions.

As key cofactors for many metabolic reactions, such as glycolysis, the TCA cycle and fatty acid β-oxidation, NAD^+ and its reduced form NADH play central roles in mammalian energy metabolism, while the conversion between these two forms drives the production of ATP *via* anaerobic glycolysis and mitochondrial OXPHOS [66]. NAD^+ is also a co-substrate of many regulatory enzymes, including sirtuins, CD38 and PARPs, directly and indirectly influencing many key cellular functions including DNA repair, chromatin remodeling and cellular senescence [12]. The SoNar sensor is unique as its fluorescence sensitively responds to the binding of NAD^+ or NADH and the read-out reflects the NAD^+/NADH ratio rather than the absolute concentrations of the two nucleotides intracellularly, thus serving a powerful tool for NAD^+/NADH detection and bioimaging. In this study, we observed a significantly decreased NAD^+/NADH ratio as revealed by the SoNar sensor, a trend indicative of markedly increased glycolytic activity and enhanced mitochondrial OXPHOS,

events correlated with an active conversion from NAD^+ towards NADH. Importantly, such a remarkable change in NAD^+/NADH ratio is accompanied by a significant increase of cytosolic lactate level in senescent cells. The capacity of lactate production is usually maintained homeostatically for proper functioning of organisms, while lactate accumulation in the TME can result in transcriptional alterations of genes correlated with cell fate regulation and phenotypic modulation [67]. We noticed a significant enhancement of lactate production upon cellular senescence, as indicated by FiLa sensor, a case reflecting intracellular lactate accumulation under experimental conditions. As expected, the FiLa sensor responds well to lactate fluctuations in different contexts, providing a unique yet powerful tool for monitoring live-cell lactate levels, which is physiologically, or in certain settings, pathophysiologically relevant as a key metabolic indicator or regulator of energy metabolism. Changes of both NAD^+/NADH metabolism and lactate production appeared to be intimately correlated with PDK4 activity, further substantiating the critical role of this enzyme in shaping the activity of senescent cells, which exhibit a metabolic spectrum markedly distinct from that of their proliferating counterparts.

ROS cover several subspecies, including superoxide anion (O_2^-), hydrogen peroxide (H_2O_2), and hydroxyl radical (OH·), which are generated as byproducts of aerobic metabolism. The major site of cellular ROS production is the mitochondria *via* its electron transport chain reaction [68]. Various NOX isoforms appear heterogeneously in a wide variety of cells type and tissues, while these enzymes are specialized in the deliberate production of ROS [69]. Although cells have evolved an anti-oxidant defense system to eliminate harmful ROS, excess ROS do override the cellular anti-oxidant defense framework and cause oxidative damage to various macromolecules, a mechanism that underlies the pathogenesis of diverse disorders and organismal aging [70]. Our data suggests the implication of NOX1 in modulating production of ROS by senescent cells, illustrating an alternative but important source of senescence-associated stress signals, which can be generated *via* such a positive feedback involving NOX1-activating lactate, a metabolite that can be derived through either an autocrine or a paracrine manner in the microenvironment harboring senescent cells. Indeed, an increased ROS level can trigger a modification of cellular redox balance in favor of overall oxidation. Consequently, multiple components of the cell will undergo acute ROS-

mediated damage, further promoting the generation of damaging signals, markedly compromising the structural and functional integrity of proteins, lipids, particularly nucleic acids, ultimately contributing to chronic inflammation characteristic of cellular senescence and underpinning many neurodegenerative, cardiovascular, and metabolic conditions [71, 72]. Although PDK4 expression may represent a cell non-autonomous process in senescent cells, the impact of resulting lactate on senescence through inducing superoxide generation and deteriorating DNA damage, events culminating in the enhanced SASP expression, does accelerate aging and organ degeneration. To the contrary, therapeutically targeting such a ROS-mediated pathological process holds the potential to antagonize organismal aging, control age-related chronic disorders and even prolong lifespan [51, 52, 73].

Metabolism plays an important role in regulating cellular senescence, a process that dramatically affects the aging process [74]. By metabolic profiling and functional assessments of the glucose consumption axis, we hereby mapped the metabolic landscape of human senescent cells, and propose that PDK4, a PDH-modifying enzyme, acts as a key regulator of biochemical activities to shape a unique form of metabolism, namely hypercatabolism, upon cellular senescence. Accumulation of senescent cells is a major cause of age-related inflammation and predisposes the host to a number of age-related pathologies. The observation that PDK4 activity is induced during senescence and plays a critical role in promoting natural aging and contributing to age-related physical dysfunction, underscores this enzyme as a valuable target to counteract the overall pathological impact of senescent cells. Chronological age-associated cellular senescence in the tissue microenvironment bridges the gap between high lactate levels, chronic inflammation and pathological events, while accumulation of lactate in solid organs is a pivotal and early event in various diseases [75, 76]. Given that high PDK4 expression rewires energy metabolism, holds the potential to cause tissue homeostasis imbalance and overall physical dysfunction, our study raises the possibility that this metabolic kinase is pharmacologically exploited for therapeutic intervention of natural aging and multiple age-related disorders, including but not limited to cancer.

Methods

Cell culture. Primary normal human prostate stromal cell line PSC27 and breast stromal cell line HBF1203 were generously provided by Dr. Peter Nelson (Fred Hutchinson Cancer Research Center) and maintained in stromal complete medium as described previously [21]. Human fetal lung stromal lines WI38 and HFL1, and foreskin stromal line BJ were from ATCC and cultured with F-12K medium supplemented with 10% FBS. Prostate cancer epithelial cell lines PC3, DU145, LNCaP and VCaP, as well as breast cancer cell line MDA-MB-231 (ATCC) were routinely cultured with RPMI 1640 (10% FBS). Prostate cancer epithelial line M12 was a kind gift from Dr. Stephen Plymate (University of Washington), which originally derived from the benign line BPH1 but phenotypically neoplastic and metastatic [77]. All lines were routinely tested for mycoplasma contamination and authenticated with STR assays.

Vectors, viruses and infection. Full length human *p16^{INK4a}*, *HRas^{G12V}* and *PDK4* sequences (forward: ATATGGATCCGCCGCCATGAAGGCGGCCCGCTTCG; reverse: CGCGCGCGTCTAGATCACATGGCCACTTCTTTTGCCAGG) was cloned into pLenti-CMV/To-Puro-DEST2 (Invitrogen), individually, as described [21]. Small hairpin RNAs (shRNA) targeting sequences for specific genes were cloned in pLKO.1-Puro vector (Addgene) (#1 set, forward: CCGGCTTTGTCTTCTGAGTCTATAGCTCGAGCTATAGACTCAGAAGACAAAGTTTTTG, reverse: AATTCAAAAACTTTGTCTTCTGAGTCTATAGCTCGAGCTATAGACTCAGAAGACAAAG; #2 set, forward: CCGGCCGCCTCTTTAGTTATACATACTCGAGTATGTATAACTAAAGAGGCGGTTTTTG, reverse: AATTCAAAAACCGCCTCTTTAGTTATACATACTCGAGTATGTATAACTAAAGAGGCGG). Upon production by 293T cells, lentivirual titers were adjusted to infect ~ 90% of cells. Stromal cells were infected overnight in the presence of polybrene (8 μg/ml), allowed to recover for 48 h and selected for 72 h before used for further analysis. For expression of

target genes in either stromal or epithelial cells, total RNA was prepared and subject to qRT-PCR assays (primers listed in Supplementary Table 2, Supporting Information).

Cell treatments. Stromal cells were grown until 80% confluent (CTRL) and treated with 50 μg/ml bleomycin (BLEO), 5 μM doxorubicin (DOX), 2 μM mitoxantrone (MIT), 50 nM docetaxel (DTX), 50 μM paclitaxel (PTX) or 20 μM vinblastine (VBL). After treatment, the cells were rinsed briefly with PBS and allowed to stay for 7-10 days prior to performance of various examinations. For experimental assays involving PDK4 inhibition, the anthraquinone derivative PDK4-IN was used at 5 μM. For MCT1/4 dual inhibition, syrosingopine was used at 10 μM. To induce mitochondrial dysfunction, rotenone (10 μM) or CCCP (10 μM) were employed. To enhance ROS production, the chemical lactate (10 mM) was applied.

Human cancer patient recruitment and biospecimen analysis. Administration of chemotherapeutic agents was performed for primary PCa patients (Clinical trial no. NCT03258320) and infiltrating ductal BCa patients (NCT02897700), by following the CONSORT 2010 Statement (updated guidelines for reporting parallel group randomized trials). Patients with a clinical stage ≥ I subtype A (IA) (T1a, N0, M0) of primary cancer but without manifest distant metastasis were enrolled into the multicentred, randomized, double-blinded and controlled pilot studies. Age between 40-75 years with histologically proven PCa, or age ≥ 18 years with histologically proven infiltrating ductal BCa was required for recruitment into the clinical cohorts. Data regarding tumor size, histologic type, tumor penetration, lymph node metastasis, and TNM stage were obtained from the pathologic records. Tumors were processed as FFPE biospecimens and sectioned for histological assessment, with alternatively prepared OCT-frozen chunks processed *via* lase capture microdissection (LCM) for gene expression analysis. Specifically, stromal compartments associated with glands and adjacent to cancer epithelium were separately isolated from tumor biopsies before and after chemotherapy using an Arcturus (Veritas Microdissection) laser capture microscope following previously defined criteria [21]. The immunoreactive scoring (IRS) gives a range of 1-4 qualitative scores according to staining

intensity *per* tissue sample. Categories for the IRS include 0-1 (negative), 1-2 (weak), 2-3 (moderate), 3-4 (strong) [78]. The diagnosis of PCa and BCa tissues was confirmed based on histological evaluation by independent pathologists. Randomized control trial (RCT) protocols and all experimental procedures were approved by the Institutional Review Board of Shanghai Jiao Tong University School of Medicine, with methods carried out in accordance with the official guidelines. Informed consent was obtained from all subjects and the experiments conformed to the principles set out in the WMA Declaration of Helsinki and the Department of Health and Human Services Belmont Report.

Histology and immunohistochemistry. Formalin-fixed paraffin-embedded (FFPE) tissue sections of 7-10 μm were deparaffinized in xylenes and rehydrated through a graded series of alcohols. Routine histology appraisal was performed with hematoxylin and eosin staining. For immunohistochemical (IHC) evaluation, FFPE sections experienced antigen retrieval with sodium citrate, incubation with 3% H_2O_2, treatment with avidin/biotin blocking buffer (Vector Laboratories) and then 3% BSA for 30 min. Staining with primary and secondary antibodies was conducted at 4°C for overnight and at room temperature for 60 min, respectively. Sections were incubated with a H_2O_2-diaminobenzidine (DAB) substrate kit (Vector, SK-4100). Samples were counterstained with hematoxylin, dehydrated and mounted. IHC images were obtained using an upright microscope (Olympus BX51). Brown staining indicated the immunoreactivity of samples.

RNA-seq and bioinformatics analysis. Total RNA samples were obtained from PC3 and DU145 cells cultured with CM of either $PSC27^{Vector}$ or $PSC27^{PDK4}$. Sample quality was validated by Bioanalyzer 2100 (Agilent), and RNA was subjected to sequencing by Illumina NovaSeq 6000 with gene expression levels quantified by the software package RSEM (https://deweylab.github.io/RSEM/). Briefly, rRNAs in the RNA samples were eliminated using the RiboMinus Eukaryote kit (Qiagen, Valencia, CA, USA), and strand-specific RNA-seq libraries were constructed using the TruSeq Stranded Total RNA preparation kits (Illumina, San Diego, CA, USA) according to the manufacturer's instructions before deep sequencing.

Pair-end transcriptomic reads were mapped to the reference genome (GRCh38.p13) (http://asia.ensembl.org/Homo_sapiens/Info/Index) (ensembl_105) with reference annotation from Gencode v27 using the Bowtie tool. Duplicate reads were identified using the picard tools (1.98) script mark duplicates (https://github.com/broadinstitute/picard) and only non-duplicate reads were retained. Reference splice junctions are provided by a reference transcriptome (Ensembl build 73) [79]. FPKM values were calculated using Cufflinks, with differential gene expression called by the Cuffdiff maximum-likelihood estimate function [80]. Genes of significantly changed expression were defined by a false discovery rate (FDR)-corrected *P* value < 0.05. Only ensembl genes 73 of status "known" and biotype "coding" were used for downstream analysis.

Reads were trimmed using Trim Galore (v0.3.0) (http://www.bioinformatics.babraham.ac.uk/projects/trim_galore/) and quality assessed using FastQC (v0.10.0) (http://www.bioinformatics.bbsrc.ac.uk/projects/fastqc/). Differentially expressed genes were subsequently analyzed for enrichment of biological themes using the DAVID bioinformatics platform (https://david.ncifcrf.gov/), the Ingenuity Pathways Analysis program (http://www.ingenuity.com/index.html). Raw data of RNA-seq were deposited in the NCBI Gene Expression Omnibus (GEO) database under the accession code GSE198110, GSE217808 and GSE222279.

Venn diagrams

Venn diagrams and associated empirical *P*-values were generated using the USeq (v7.1.2) tool IntersectLists [81]. The t-value used was 22,008, as the total number of genes of status "known" and biotype "coding" in ensembl genes 73. The number of iterations used was 1,000.

RNA-seq heatmaps

For each gene, the FPKM value was calculated based on aligned reads, using Cufflinks [80]. Z-scores were generated from FPKMs. Hierarchical clustering was performed using the

R package heatmap.2 and the distfun = “pearson” and hclustfun = “average”.

Immunoblot and immunofluorescence analysis. Whole cell lysates were prepared using RIPA lysis buffer supplemented with protease/phosphatase inhibitor cocktail (Biomake). Nitrocellulose membranes were incubated overnight at 4°C with primary antibodies listed in Table S6, Supporting Information, and HRP-conjugated goat anti-mouse or -rabbit served as secondary antibodies (Vazyme). For immunofluorescence analysis, cells were fixed with 4% formaldehyde and permeabilized before incubation with primary and secondary antibodies, each for 1 hr. Upon counterstaining with DAPI (0.5 μg/ml), samples were examined with an Imager A2. Axio (Zeiss) upright microscope to analyze specific gene expression.

In vitro **cell phenotypic characterization.** For proliferation assays of cancer cells, 2×10^4 cells were dispensed into 6 well-plates and co-cultured with conditioned medium (CM) from stromal cells. Three days later, cells were digested and counted with hemacytometer. For migration assays, cells were added to the top chambers of transwells (8 μm pore), while stromal CM were given to the bottom. Migrating cells in the bottom chambers were stained by DAPI 12-24 hr later, with samples examined with an Observer A1. Axio (Zeiss) inverted microscope. Invasion assays were performed similarly with migration experiments, except that transwells were coated with basement membrane matrix (phenol red free, Corning). Alternatively, cancer cells were subject to wound healing assays conducted with 6-well plates, with healing patterns graphed with bright field microscope. For chemoresistance assays, cancer cells were incubated with stromal CM, with the chemotherapeutic agent MIT provided in wells for 3 days at each cell line’s IC50, a value experimentally predetermined. Cell viability was assayed by a CCK-8 kit, with the absorbance at 450 nm measured using a microplate reader.

Metabolic analysis. Extracellular acidification rate (ECAR) was measured with a Glycolysis Stress Test kit (Agilent Technologies, 103020-100), while oxygen consumption rate (OCR) assessed using a Cell Mito Stress Test kit (Agilent Technologies, 103015-100). ECAR and OCR were determined with an XF24 Extracellular Flux Analyzer (Seahorse

Bioscience, North Billerica, MA, 01862) according to the manufacturer's standard protocol. PSC27 was seeded at a density of 5×10^4 cells/ well in the XF24 cell culture microplate (Agilent Technologies, 04721 and Q01321) at a 37°C 5% CO_2 incubator for overnight. To measure ECAR, 10 mM glucose, 1 μM oligomycin and 50 mM 2-DG were injected into each well. To measure the OCR, 1.5 μM oligomycin, 0.5 μM carbonyl cyanide 4-(trifluoromethoxy) phenylhydrazone (FCCP) and 0.5 μM rotenone/antimycin were injected sequentially in order into each well. All Seahorse data were normalized with cell numbers. All metabolic parameters are automatically calculated by WAVE software equipped in the Seahorse. Each value was calculated as follows. Non-glycolytic acidification was referred to as last rate measurement prior to glucose injection. Glycolysis rate was referred to as maximum rate measurement before Oligomycin injection - last rate measurement before glucose injection. Glycolytic capacity was referred to as maximum rate measurement after Oligomycin injection - last rate measurement before glucose injection. For the OCR, basal respiration was referred to as last rate measurement before first injection - minimum rate measurement after Rotenone/Antimycin injection. ATP production was referred to as last rate measurement before Oligomycin injection - minimum rate measurement after Oligomycin injection.

Metabolite labelling and measurement by GC-MS. Cells were resuspended in 0.6 ml cold (-40 °C) 50% aqueous methanol containing 100 μM norvaline as an internal standard, inserted in dry ice for 30 mins for thawing. Samples were added with 0.4 ml chloroform and vortexed for 30 second before centrifugation at 14,000 rpm (4 °C) for 10 min, with supernatant transferred to new 1.5 ml tubes for evaporation before stored at -80°C. Metabolites were processed for GC/MS analysis as follows: First, 70 μl of pyridine was added to the dried pellet and incubated for 20 min at 80 °C. After cooling, 30 μl of *N-tert*-butyldimethylsilyl-*N*-methyltrifluoroacetamide (Sigma) was added, with samples re-incubated for 60 min at 80 °C before centrifugation for 10 min at 14,000 rpm (4 °C). The supernatant was transferred to an autosampler vial for GC-MS analysis. A Shimadzu QP-2010 Ultra gas chromatography-mass spectrometry (GC-MS) was programmed with an injection temperature of 250°C and injected with 1 μl samples. GC oven temperature

started at 110 °C for 4 min, before raised to 230 °C at 3 °C/min and to 280 °C at 20 °C /min with a final hold at this temperature for 2 min. GC flow rate with helium carrier gas was 50 cm/s, with the GC column used at 20 m x 0.25 mm x 0.25 mm Rxi-5ms. GC-MS interface temperature was 300°C, while ion source temperature (electron impact) was set at 200 °C with 70 V ionization voltage. The mass spectrometer was set to scan m/z range 50-800 with 1 kV detector.

GC-MS data were analyzed to determine isotope labeling. To determine ^{13}C labeling, the mass distribution for known fragments of metabolites was extracted from the appropriate chromatographic peak. These fragments contained either the whole carbon skeleton of the metabolite, or lacked the alpha carboxyl carbon, or (for some amino acids) contained only the backbone minus the side-chain. For each fragment, the retrieved data comprised mass intensities for the lightest isotopomer (without any heavy isotopes, M0) and isotopomers with increasing unit mass (M1 to M6) relative to M0. These mass distributions were normalized by dividing by the sum of M0 to M6 and corrected for the natural abundance of heavy isotopes of the elements H, N, O, Si and C, using matrix-based probabilistic methods and implemented in MATLAB. Labeling results are expressed as average fraction the particular compound containing isotopic label from the particular precursor.

Lactate assay. Lactate production was measured using a Lactate Colorimetric Assay Kit (Sigma-Aldrich, MAK058). Cells were homogenized in lactate assay buffer and centrifuged at 13,000 x g for 10 min to remove insoluble materials. The supernatants were de-proteinized with a 10 kDa MWCO spin filter to remove other enzymes. Next, 50 ml of the supernatants was mixed with 50 ml of the reaction mix, with the reaction incubated for 30 min at room temperature. Lactate levels were measured at 450 nm using a microplate reader, with the relative level of lactate in all groups calculated and normalized to protein concentration.

Glucose uptake assay. The level of glucose uptake was measured using a Glucose Uptake-Glo Assay Kit (Promega, J1341), which provided a homogeneous bioluminescent method

for assessing glucose uptake in mammalian cells based on the detection of 2-deoxyglucose-6-phosphate (2DG-6-P). Cells were removed from medium and then washed with PBS, afterwards 50 ml of 1mM 2-deoxyglucose (2DG) was added to the cells and incubated for 10 min at room temperature. Then 25 ml of acid detergent solution (stop buffer) was added to lyse the cells and terminate the uptake; 25 ml of high-pH buffer solution (neutralization buffer) was then added to neutralize the acid. Finally, 100 ml of 2DG-6-P detection reagent was added to the sample wells, with the reaction incubated at room temperature for 1-2 h. A Cytation 5 Cell Imaging Multi-Mode Reader was used to assay the luminescence. The relative level of glucose uptake in all groups was calculated and normalized to protein concentration.

Characterization of SoNar and FiLa *in vitro*. Purified protein was stored at -80 °C before experimental assays. For *in vitro* measurements, the purified sensor protein was diluted with 100 mM HEPES buffer containing 100 mM NaCl (pH 7.4). Fluorescence spectroscopy was performed on a fluorescence spectrophotometer (PerkinElmer, FL6500). Excitation spectra were recorded at an emission wavelength of 530 nm. Slit width was set as 10 nm bandpass and the PMT voltage was set at 500 V.

For nucleotide titration of SoNar and lactate titration of FiLa, the sensor protein was diluted in HEPES buffer (pH 7.4) to a final concentration of 0.2 μM. The fluorescence intensity was measured by a filter-based Synergy Neo 2 Multi-Mode microplate reader using 420 BP 20 nm or 485 BP 20 nm excitation and 532 BP 40 nm emission band-pass filters (BioTek). All solutions were prepared in HEPES buffer (pH 7.4). Each assay was performed in a 96-well black bottom plate using 50 μl of substrate and 50 μl of sensor protein. Fluorescence intensity was measured immediately.

Live-cell fluorescence imaging. For fluorescence imaging, normal and senescent (TIS) PSC27 cells stably expressing SoNar, FiLa, iNapc or FiLa-C were plated on 35 mm 4-chamber glass-bottom dish. The dosing group was treated with or without 5 μM PDK inhibitor for 1 h. Fluorescence images were acquired using a Leica TCS SP8 SMD confocal laser-scanning microscope system with HC Plan Apo CS2 63×1.40 NA oil objective. For

dual-excitation ratio imaging, 405 nm excitation laser and 488 nm excitation laser with an emission range of 500-550 nm were used. Raw data were exported to ImageJ software as 12-bit TIF for analysis. The pixel-by-pixel ratio of the 405 nm excitation image by the 488 nm excitation image of the same cell was used to pseudo-color the images in HSB color space as previously described [36, 82].

Experimental animals and chemotherapeutic studies. All animals were maintained in a specific pathogen-free (SPF) facility, with NOD/SCID (Charles River and Nanjing Biomedical Research Institute of Nanjing University) mice at an age of approximately 6 weeks (~20 g body weight) used. Ten mice were incorporated in each group, and xenografts were subcutaneously generated at the hind flank upon anesthesia mediated by isoflurane inhalation. Stromal cells (PSC27 or HBF1203) were mixed with cancer cells (PC3, LNCaP or MDA-MB-231) at a ratio of 1:4 (i.e., 250,000 stromal cells admixed with 1,000,000 cancer cells to make tissue recombinants before implantation *in vivo*). Animals were sacrificed at 2-8 weeks after tumor xenografting, according to tumor burden or experimental requirements. Tumor growth was monitored weekly, with tumor volume (v) measured and calculated according to the tumor length (l), width (w) and height (h) by the formula: $v = (\pi/6) \times ((l+w+h)/3)^3$ [44]. Freshly dissected tumors were either snap-frozen or fixed to prepare FFPE samples. Resulting sections were used for IHC staining against specific antigens or subject to hematoxylin/eosin staining.

For chemoresistance studies, animals received subcutaneous implantation of tissue recombinants as described above and were given standard laboratory diets for 2 weeks to allow tumor uptake and growth initiation. Starting from the 3rd week (tumors reaching 4-8 mm in diameter), MIT (0.2 mg/kg doses), DOX (doxorubicin, 1.0 mg/kg doses), therapeutic agent PDK4-IN (10.0 mg/kg doses, 200 μl/dose) or vehicle controls was administered by intraperitoneal injection (therapeutic agents *via* i.p. route), on the 1st day of 3rd, 5th and 7th weeks, respectively. Upon completion of the 8-week therapeutic regimen, animals were sacrificed, with tumor volumes recorded and tissues processed for histological evaluation.

At the end of chemotherapy and/or targeting treatment, animals were anaesthetized and peripheral blood was gathered *via* cardiac puncture. Blood was transferred into a 1.5 ml Eppendorf tube and kept on ice for 45 min, followed by centrifugation at 9000 x g for 10 min at 4 ˚C. Clear supernatants containing serum were collected and transferred into a sterile 1.5 ml Eppendorf tube. All serum markers were measured using dry-slide technology on IDEXX VetTest 8008 chemistry analyzer (IDEXX). About 50 μl of the serum sample was loaded on the VetTest pipette tip before securely fit on the pipettor and manufacturer's instructions were followed for further examination.

All animal experiments were performed in compliance with NIH Guide for the Care and Use of Laboratory Animals (National Academies Press, 2011) and the ARRIVE guidelines, and were approved by the Institutional Animal Care and Use Committee (IACUC) of Shanghai Institute of Nutrition and Health, Chinese Academy of Sciences.

Senescent cell targeting and lifespan studies. For age-related studies, wildtype (WT) C57BL/6J male mice were maintained in a specific pathogen-free (SPF) facility at 22-25 °C under a 12 h/12 h light/dark cycle (08:00 to 20:00 light on), with free access to food (standard mouse diet, Lab Diet 5053) and water provided *ad libitum*. The experimental procedure was approved by the IACUC at Shanghai Institute of Nutritional and Health, Chinese Academy of Sciences, with all animals conducted in accordance with the guidelines for animal experiments defined by the IACUC.

For preclinical studies of natural ageing, 20-month-old non-transplanted WT C57BL/6J mice (males) were used, which were generally sorted according to their body weight and randomly assigned to vehicle, PDK4-IN or PCC1 treatment. Animals were treated once every 2 weeks, in an intermittent manner for 4 months before physical tests at 24 months of age. For intervention trials involving lifespan extension at advanced age, we used animals at a very old age. Starting at 24-27 months of age (equivalent to human age of 75-90 years), mice (both sexes) were treated once every 2 weeks (biweekly) with vehicle, PDK4-IN or PCC1 through i.p. injection (10.0 mg/kg and 20.0 mg/kg doses for PDK4-IN

and PCC1, respectively) for 3 consecutive days. Some mice were moved from their original cages during the study to minimize single cage-housing stress. RotaRod (TSE system, Chesterfield, MO) and hanging tests were chosen for monthly measurement of maximal speed and hanging endurance, respectively, as these tests are considered sensitive and noninvasive. Animals were euthanized and scored as having died if displaying more than one of the following signs: (i) incapable to drink or eat; (ii) reluctant to move even upon stimulus; (iii) rapid weight loss; (iv) severe balance disorder; or (v) bleeding or ulcerated skin. No mouse was lost due to fighting, accidental death, or dermatitis. The Cox proportional hazard model was used for survival appraisal.

Postmortem pathological examination. Mouse cages were checked every day, with dead animals removed from cages. Within 24 h, corpses were opened (abdominal cavity, thoracic cavity and skull) and preserved in 4% paraformaldehyde (PFA) individually for at least 7 d， with decomposed or disrupted bodies excluded. The preserved bodies were rendered to pathologists for blinded examination, following an assessment routine. Briefly, tumour burden (sum of different types of tumours in each mouse), disease burden (sum of different histopathological changes of major organs in each mouse), severity of each lesion, and inflammation (lymphocytic infiltrate) were assessed.

Physical function appraisal. All physical tests were performed at least 5 d after the last dose of drug treatment. Maximal walking speed was measured using an accelerating RotaRod system (TSE system, Chesterfield, MO). Briefly, animals were trained on the RotaRod for 3 d at speeds of 4, 6, and 8 rpm for 200 sec on days 1, 2, and 3 for coordination test. On the test day, mice were placed onto the RotaRod, which was started at 4 rpm. The rotating speed was accelerated from 4 to 40 rpm over a 5-min interval. The speed was recorded when the mouse dropped off the RotaRod, with results averaged from 3 or 4 trials and normalized to baseline speed. Training was not repeated for mice that had been trained within the preceding 2 months. The average values of each mouse were used for statistical inference.

Forelimb grip strength (N) was determined using a Grip Strength Meter (Columbus Instruments), with results averaged over ten trials. To measure grip strength the mouse is swung gently by the tail so that its forelimbs contact the bar. The mouse instinctively grips the bar and is pulled horizontally backwards, exerting a tension. When the tension becomes overwhelming, the mouse releases the bars. For the hanging test, mice were placed onto a 2-mm-thick metal wire that was 35 cm above a padded surface, while animals were allowed to grab the wire with their forelimbs only. Hanging time was normalized to body weight as hanging duration (sec) × body weight (g), with results averaged from 2 or 3 trials for each mouse. A Comprehensive Laboratory Animal Monitoring System (CLAMS, Columbus Instruments) was used to monitor daily activity and food intake over a 24-h period (12-h light/12-h dark). The CLAMS system was equipped with an Oxymax Open Circuit Calorimeter System (Columbus Instruments). For treadmill performance, mice were acclimated to a motorized treadmill at an incline of 5° (Columbus Instruments) over 3 d for 5 min each day, starting at a speed of 5 m/min for 2 min and progressing to 7 m/min for 2 min and then 9 m/min for 1 min. On the test day, mice ran on the treadmill at an initial speed of 5 m/min for 2 min, and then the speed was increased by 2 m/min every 2 min until the mice were exhausted. The speed when the mouse dropped from the RotaRod was recorded, and results were averaged from three tests. Exhaustion was defined as the inability to return onto the treadmill despite a mild electrical shock stimulus and mechanical prodding. Distance was recorded and total work (KJ) was calculated using the following formula: mass (kg) × g (9.8 m/s^2) × distance (m) × sin (5°).

In a subset of 8-10 mice *per* group, habitual ambulatory, rearing, and total activity, oxygen consumption (VO_2), and carbon dioxide production (VCO_2) of individual animal were monitored over a 24-h period (12 h light/12 h dark) using the CLAMS system equipped with an Oxymax Open Circuit Calorimeter System (Columbus Instruments). Ambulatory, rearing, and total activities were summed and analyzed for light and dark periods under fed conditions. The VO_2 and VCO_2 values were used to calculate the respiratory exchange ratio (RER) and VO_2. RER values were used to determine the basal metabolic rate (in kilocalories per kilogram *per* hour).

Tissue SA-β-Gal staining and histological examination. For SA-β-Gal staining, frozen sections were dried at 37 °C for 20-30 min before fixed for 15 min at room temperature. The frozen sections were washed thrice with PBS and incubated with SA-β-Gal staining reagent (Beyotime) overnight at 37 °C. After completion of SA-β-Gal staining, sections were stained with eosin for 1-2 min, rinsed under running water for 1 min, differentiated in 1% acid alcohol for 10-20 s, and washed again under running water for 1 min. Sections were dehydrated in increasing concentrations of alcohol and cleared in xylene. After drying, samples were examined under a bright-field microscope.

Liver, lung, prostate and cardiac tissue frozen sections stained with SA-β-Gal were quantified by ImageJ software (NIH) to measure the SA-β-Gal$^+$ area. The total region was quantified by eosin-positive area, while relative quantities of SA-β-Gal$^+$ cells were calculated with the SA-β-Gal$^+$ area divided by the total area. For the statistics of SA-β-Gal$^+$ area of lung, regions of lung were randomly selected to be photographed, avoiding analysis of larger pulmonary blood vessels and the trachea. For statistical analysis of SA-β-Gal-positive area of the liver, regions were randomly selected to be photographed. Each tissue was measured over 10-15 regions. The stained tissue sections were then observed with an Eclipse Ti-S (Nikon) microscope under bright-field illumination. For histochemical staining of the lung, tissues were preserved in OCT compound before cryo-sectioned and stained with H&E reagents. To quantify the alveolar size *via* ImageJ, we defined the areas with the Huang threshold and then measured average areas greater than 1,500 and 2,000 and 40 pixels, respectively, in 3 fields for each section.

***In vivo* cytotoxicity evaluation by blood tests.** For routine blood examination, 100 μl fresh blood was acquired from each animal and mixed with EDTA immediately. The blood samples were analyzed with Celltac Alpha MEK-6400 series hematology analyzers (Nihon Kohden). For serum biochemical analyses, blood samples were collected and clotted for 2 h at room temperature or overnight at 4 °C. Samples were then centrifuged (1000 × g, 10 min) to obtain serum. An aliquot of approximately 50 μl serum was subjected to analysis for creatinine, urea, alkaline phosphatase (ALP) and alanine transaminase (ALT) by an

automatic biochemical analyzer (BS-5800M, Mindray Bio-Medical Electronics Co. Ltd). Evaluation of circulating levels of hemoglobin, white blood cells, lymphocytes and platelets were performed using dry-slide technology on a VetTest 8008 chemistry analyzer (IDEXX) as reported previously [44].

All animal experiments were conducted in compliance with the NIH Guide for the Care and Use of Laboratory Animals (National Academies Press, 2011) and the ARRIVE guidelines, and were approved by the IACUC of Shanghai Institute of Nutrition and Health, Chinese Academy of Sciences. For each preclinical regimen, animals were monitored for conditions including hypersensitivity (changes in body temperature, altered breathing and ruffled fur), body weight, mortality, and changes in behavior (i.e., loss of appetite and distress), and were disposed of appropriately according to the individual pathological severity as defined by relevant guidelines.

Measurement of AST, ALT and LDH levels in serum. Circulating blood was taken from mice through cardiac puncture and left at room temperature for 15 min. To obtain serum, blood samples were centrifuged at 3,500 *g* for 15 min at 4 °C. Any serum sample with severe haemolysis was excluded from further analyses of AST, ALT and LDH. Serum levels of AST, ALT and LDH were examined individually by commercial kits (Mindray).

Assessment of lipid peroxidation. The levels of 4-hydroxynonenal (HNE)-protein adducts in liver tissue lysates prepared in RIPA buffer were assessed in livers of mice using the OxiSelect HNE Adduct Competitive ELISA Kit (Cell Biolabs, San Diego, CA), as formerly described [83].

Appraisal of glutathione. Mouse livers fixed in 5% sulfosalicylic acid were prepared and analyzed for the concentration of reduced (GSH) and oxidized (GSSG) glutathione using a Glutathione Assay Kit (Cayman Chemical, Ann Arbor, MI) as previously described [83]. Sample absorbance was detected at a wavelength of 405 nm using a plate reader and the ratio of GSH: GSSG was obtained for each tested tissue sample.

Statistics. All *in vitro* experiments were performed in triplicates, while animal studies were conducted with at least 10 mice *per* group. Data are presented as mean ± SD except where otherwise indicated. GraphPad Prism 8.4.3 was used to collect and analyze data, with statistical significance determined according to individual settings. Cox proportional hazards regression model and multivariate Cox proportional hazards model analysis were performed with statistical software SPSS. Statistical significance was determined by unpaired two-tailed Student's *t* test, one- or two-way ANOVA, Pearson's correlation coefficients test, Kruskal-Wallis, log-rank test, Wilcoxon-Mann-Whitney test or Fisher's exact test. For all statistical tests, a *P* value < 0.05 was considered significant.

To determine sample size, we began by setting the values of type I error (α) and power (1-β) to be statistically adequate: 0.05 and 0.80, respectively [84]. We then determined *n* on the basis of the smallest effect we measured. If the required sample size is too large, we chose to reassess the objectives or to more tightly control the experimental conditions to reduce variance. For mouse experiments, all mice with the same genotype were randomly assigned to each group and independently followed the same age-dependent schedule in each experimental design. We did not exclude samples or animals. Sample sizes were not predetermined by pilot studies, nor statistical methods used to predetermine sample sizes, which, however, were similar to those generally employed in relevant fields. Blind designs were not involved in this study because of the automatic analyses obtained using the image analyzer with the same criteria.

Data availability

Data supporting the plots within this paper and other findings of this study are available from the corresponding author upon reasonable request. The RNA-seq data generated in the present study have been deposited in the Gene Expression Omnibus database under accession codes GSE198110, GSE217808 and GSE222279.

References

1. Hayflick, L. & Moorhead, P.S. The serial cultivation of human diploid cell strains. *Exp Cell Res* **25**, 585-621 (1961).
2. Di Micco, R., Krizhanovsky, V., Baker, D. & d'Adda di Fagagna, F. Cellular senescence in ageing: from mechanisms to therapeutic opportunities. *Nat Rev Mol Cell Biol* **22**, 75-95 (2021).
3. Wiley, C.D. & Campisi, J. From Ancient Pathways to Aging Cells-Connecting Metabolism and Cellular Senescence. *Cell Metab* **23**, 1013-1021 (2016).
4. Song, S., Lam, E.W., Tchkonia, T., Kirkland, J.L. & Sun, Y. Senescent Cells: Emerging Targets for Human Aging and Age-Related Diseases. *Trends in biochemical sciences* **45**, 578-592 (2020).
5. Coppe, J.P. *et al.* Senescence-associated secretory phenotypes reveal cell-nonautonomous functions of oncogenic RAS and the p53 tumor suppressor. *PLoS biology* **6**, 2853-2868 (2008).
6. Sieben, C.J., Sturmlechner, I., van de Sluis, B. & van Deursen, J.M. Two-Step senescence-focused cancer therapies. *Trends in cell biology* **28**, 723-737 (2018).
7. Baker, D.J. *et al.* Clearance of p16Ink4a-positive senescent cells delays ageing-associated disorders. *Nature* **479**, 232-236 (2011).
8. Baker, D.J. *et al.* Naturally occurring p16(Ink4a)-positive cells shorten healthy lifespan. *Nature* **530**, 184-189 (2016).
9. Basisty, N. *et al.* A proteomic atlas of senescence-associated secretomes for aging biomarker development. *PLoS biology* **18**, e3000599 (2020).
10. Wiley, C.D. *et al.* Mitochondrial Dysfunction Induces Senescence with a Distinct Secretory Phenotype. *Cell Metab* **23**, 303-314 (2016).
11. Nacarelli, T. *et al.* NAD(+) metabolism governs the proinflammatory senescence-associated secretome. *Nat Cell Biol* **21**, 397-407 (2019).
12. Covarrubias, A.J., Perrone, R., Grozio, A. & Verdin, E. NAD(+) metabolism and its roles in cellular processes during ageing. *Nat Rev Mol Cell Biol* **22**, 119-141 (2021).
13. Katsyuba, E., Romani, M., Hofer, D. & Auwerx, J. NAD(+) homeostasis in health and disease. *Nat Metab* **2**, 9-31 (2020).
14. Camacho-Pereira, J. *et al.* CD38 Dictates Age-Related NAD Decline and Mitochondrial Dysfunction through an SIRT3-Dependent Mechanism. *Cell Metabolism* **23**, 1127-1139 (2016).
15. Tarrago, M.G. *et al.* A Potent and Specific CD38 Inhibitor Ameliorates Age-Related Metabolic Dysfunction by Reversing Tissue NAD(+) Decline. *Cell Metab* **27**, 1081-1095 e1010 (2018).
16. Covarrubias, A.J. *et al.* Senescent cells promote tissue NAD(+) decline during ageing via the activation of CD38(+) macrophages. *Nat Metab* **2**, 1265-1283 (2020).
17. Thapa, D. *et al.* Adropin regulates pyruvate dehydrogenase in cardiac cells via a novel GPCR-MAPK-PDK4 signaling pathway. *Redox Biol* **18**, 25-32 (2018).
18. Leclerc, D. *et al.* Oncogenic role of PDK4 in human colon cancer cells. *British journal of cancer* **116**, 930-936 (2017).
19. Sun, Y. *et al.* Metabolic and transcriptional profiling reveals pyruvate dehydrogenase kinase 4 as a mediator of epithelial-mesenchymal transition and drug resistance in tumor cells. *Cancer Metab* **2**, 20 (2014).
20. Sun, S. *et al.* Loss of the novel mitochondrial protein FAM210B promotes metastasis via PDK4-dependent metabolic reprogramming. *Cell Death Dis* **8**, e2870 (2017).
21. Sun, Y. *et al.* Treatment-induced damage to the tumor microenvironment promotes prostate cancer therapy resistance through WNT16B. *Nat Med* **18**, 1359-1368 (2012).

22. Zhang, B.Y. *et al.* The senescence-associated secretory phenotype is potentiated by feedforward regulatory mechanisms involving Zscan4 and TAK1. *Nat Commun* **9**, 1723 (2018).
23. An, Y. & Duan, H. The role of m6A RNA methylation in cancer metabolism. *Mol Cancer* **21**, 14 (2022).
24. Prasanna, P.G. *et al.* Therapy-Induced Senescence: Opportunities to Improve Anticancer Therapy. *Journal of the National Cancer Institute* **113**, 1285-1298 (2021).
25. Calcinotto, A. *et al.* Cellular Senescence: Aging, Cancer, and Injury. *Physiol Rev* **99**, 1047-1078 (2019).
26. Dorr, J.R. *et al.* Synthetic lethal metabolic targeting of cellular senescence in cancer therapy. *Nature* **501**, 421-425 (2013).
27. Kaplon, J. *et al.* A key role for mitochondrial gatekeeper pyruvate dehydrogenase in oncogene-induced senescence. *Nature* **498**, 109-112 (2013).
28. Kirsch, B.J. *et al.* Metabolic analysis of the asparagine and glutamine dynamics in an industrial Chinese hamster ovary fed-batch process. *Biotechnol Bioeng* (2021).
29. Pan, Y. *et al.* Link between senescence and cell fate: Senescence-associated secretory phenotype (SASP) and its effects on stem cell fate transition. *Rejuvenation Res* (2022).
30. Davidson, S.M. *et al.* Environment Impacts the Metabolic Dependencies of Ras-Driven Non-Small Cell Lung Cancer. *Cell Metab* **23**, 517-528 (2016).
31. Martini, H. & Passos, J.F. Cellular senescence: all roads lead to mitochondria. *Febs J*, 16361 (2022).
32. Lee, D. *et al.* Discovery of Novel Pyruvate Dehydrogenase Kinase 4 Inhibitors for Potential Oral Treatment of Metabolic Diseases. *J Med Chem* **62**, 575-588 (2019).
33. Yu, H., Luo, H. & Liu, X. Knockdown of circ_0102273 inhibits the proliferation, metastasis and glycolysis of breast cancer through miR-1236-3p/PFKFB3 axis. *Anticancer Drugs* **33**, 323-334 (2022).
34. Zhang, Y., Wu, Y. & Su, X. PLOD1 promotes cell growth and aerobic glycolysis by regulating the SOX9/PI3K/Akt/mTOR signaling pathway in gastric cancer. *Front Biosci (Landmark Ed)* **26**, 322-334 (2021).
35. Zhao, Y., Zhang, Z., Zou, Y. & Yang, Y. Visualization of Nicotine Adenine Dinucleotide Redox Homeostasis with Genetically Encoded Fluorescent Sensors. *Antioxid Redox Signal* **28**, 213-229 (2018).
36. Zhao, Y. *et al.* SoNar, a Highly Responsive NAD+/NADH Sensor, Allows High-Throughput Metabolic Screening of Anti-tumor Agents. *Cell Metab* **21**, 777-789 (2015).
37. Li, X. *et al.* Ultrasensitive sensors reveal the spatiotemporal landscape of lactate metabolism in physiology and disease. *Cell Metab* **35**, 200-211 e209 (2023).
38. Mao, L. *et al.* 5-HT2B-mediated serotonin activation in enterocytes suppresses colitis-associated cancer initiation and promotes cancer progression. *Theranostics* **12**, 3928-3945 (2022).
39. Li, S. *et al.* Prediction of Synergistic Drug Combinations for Prostate Cancer by Transcriptomic and Network Characteristics. *Front Pharmacol* **12**, 634097 (2021).
40. Dueck, A.C. *et al.* Assessment of Adverse Events From the Patient Perspective in a Phase 3 Metastatic Castration-Resistant Prostate Cancer Clinical Trial. *JAMA Oncol* **6**, e193332 (2020).
41. Cathala, A. *et al.* Serotonin2B receptor blockade in the rat dorsal raphe nucleus suppresses cocaine-induced hyperlocomotion through an opposite control of mesocortical and

mesoaccumbens dopamine pathways. *Neuropharmacology* **180**, 108309 (2020).
42. Benjamin, D. *et al.* Dual Inhibition of the Lactate Transporters MCT1 and MCT4 Is Synthetic Lethal with Metformin due to NAD+ Depletion in Cancer Cells. *Cell Rep* **25**, 3047-3058 e3044 (2018).
43. Buyse, C. *et al.* Evaluation of Syrosingopine, an MCT Inhibitor, as Potential Modulator of Tumor Metabolism and Extracellular Acidification. *Metabolites* **12** (2022).
44. Chen, F. *et al.* Targeting SPINK1 in the damaged tumour microenvironment alleviates therapeutic resistance. *Nat Commun* **9**, 4315 (2018).
45. Xu, Q. *et al.* Targeting amphiregulin (AREG) derived from senescent stromal cells diminishes cancer resistance and averts programmed cell death 1 ligand (PD-L1)-mediated immunosuppression. *Aging cell* **18**, e13027 (2019).
46. Melisi, D. *et al.* Modulation of pancreatic cancer chemoresistance by inhibition of TAK1. *Journal of the National Cancer Institute* **103**, 1190-1204 (2011).
47. Cerami, E. *et al.* The cBio cancer genomics portal: an open platform for exploring multidimensional cancer genomics data. *Cancer discovery* **2**, 401-404 (2012).
48. Gao, J.J. *et al.* Integrative Analysis of Complex Cancer Genomics and Clinical Profiles Using the cBioPortal. *Science signaling* **6** (2013).
49. Li, Z. *et al.* N(6)-methyladenosine regulates glycolysis of cancer cells through PDK4. *Nat Commun* **11**, 2578 (2020).
50. Song, X. *et al.* PDK4 dictates metabolic resistance to ferroptosis by suppressing pyruvate oxidation and fatty acid synthesis. *Cell Rep* **34**, 108767 (2021).
51. Iatsenko, I., Boquete, J.P. & Lemaitre, B. Microbiota-Derived Lactate Activates Production of Reactive Oxygen Species by the Intestinal NADPH Oxidase Nox and Shortens Drosophila Lifespan. *Immunity* **49**, 929-942 e925 (2018).
52. Luo, S.T. *et al.* The Promotion of Erythropoiesis via the Regulation of Reactive Oxygen Species by Lactic Acid. *Scientific reports* **7**, 38105 (2017).
53. Ogboo, B.C. *et al.* Architecture of the NADPH oxidase family of enzymes. *Redox Biol* **52**, 102298 (2022).
54. Xu, Q.X. *et al.* The flavonoid procyanidin C1 has senotherapeutic activity and increases lifespan in mice. *Nature Metabolism* **3**, 1706-1726 (2021).
55. Wang, T.W. *et al.* Blocking PD-L1-PD-1 improves senescence surveillance and ageing phenotypes. *Nature* **611**, 358-364 (2022).
56. Ogrodnik, M. *et al.* Cellular senescence drives age-dependent hepatic steatosis. *Nat Commun* **8**, 15691 (2017).
57. Liu, Y. *et al.* Expression of p16(INK4a) in peripheral blood T-cells is a biomarker of human aging. *Aging cell* **8**, 439-448 (2009).
58. Zeng, Y. *et al.* Comparison of In Vitro and In Vivo Antioxidant Activities of Six Flavonoids with Similar Structures. *Antioxidants (Basel)* **9** (2020).
59. Rodriguez-Ramiro, I., Martin, M.A., Ramos, S., Bravo, L. & Goya, L. Comparative effects of dietary flavanols on antioxidant defences and their response to oxidant-induced stress on Caco2 cells. *Eur J Nutr* **50**, 313-322 (2011).
60. Gasek, N.S., Kuchel, G.A., Kirkland, J.L. & Xu, M. Strategies for Targeting Senescent Cells in Human Disease. *Nat Aging* **1**, 870-879 (2021).
61. Leem, J. & Lee, I.K. Mechanisms of Vascular Calcification: The Pivotal Role of Pyruvate

Dehydrogenase Kinase 4. *Endocrinol Metab (Seoul)* **31**, 52-61 (2016).
62. Li, G. *et al.* The microRNA-182-PDK4 axis regulates lung tumorigenesis by modulating pyruvate dehydrogenase and lipogenesis. *Oncogene* **36**, 989-998 (2017).
63. Wang, J.H., Qian, Y. & Gao, M.Y. Overexpression of PDK4 is associated with cell proliferation, drug resistance and poor prognosis in ovarian cancer. *Cancer Management and Research* **11**, 251-262 (2019).
64. Wu, J. *et al.* Loss of PDK4 switches the hepatic NF-kappaB/TNF pathway from pro-survival to pro-apoptosis. *Hepatology* **68**, 1111-1124 (2018).
65. Delfarah, A. *et al.* Inhibition of nucleotide synthesis promotes replicative senescence of human mammary epithelial cells. *The Journal of biological chemistry* **294**, 10564-10578 (2019).
66. Fang, E.F. *et al.* NAD(+) in Aging: Molecular Mechanisms and Translational Implications. *Trends Mol Med* **23**, 899-916 (2017).
67. Guo, X. *et al.* NAD(+) salvage governs mitochondrial metabolism, invigorating natural killer cell antitumor immunity. *Hepatology* (2022).
68. Kudryavtseva, A.V. *et al.* Mitochondrial dysfunction and oxidative stress in aging and cancer. *Oncotarget* **7**, 44879-44905 (2016).
69. Vermot, A., Petit-Hartlein, I., Smith, S.M.E. & Fieschi, F. NADPH Oxidases (NOX): An Overview from Discovery, Molecular Mechanisms to Physiology and Pathology. *Antioxidants (Basel)* **10** (2021).
70. Park, S., Kim, B.K. & Park, S.K. Effects of Fisetin, a Plant-Derived Flavonoid, on Response to Oxidative Stress, Aging, and Age-Related Diseases in Caenorhabditis elegans. *Pharmaceuticals (Basel)* **15** (2022).
71. Liu, Y. *et al.* Embryonic stem cell extracellular vesicles reverse the senescence of retinal pigment epithelial cells by the p38MAPK pathway. *Exp Eye Res*, 109365 (2022).
72. Han, J., Park, D., Park, J.Y. & Han, S. Inhibition of NADPH Oxidases Prevents the Development of Osteoarthritis. *Antioxidants (Basel)* **11** (2022).
73. Wei, Y., Jia, S., Ding, Y., Xia, S. & Giunta, S. Balanced basal-levels of ROS (redox-biology), and very-low-levels of pro-inflammatory cytokines (cold-inflammaging), as signaling molecules can prevent or slow-down overt-inflammaging, and the aging-associated decline of adaptive-homeostasis. *Experimental gerontology* **172**, 112067 (2022).
74. Ren, R., Ocampo, A., Liu, G.H. & Izpisua Belmonte, J.C. Regulation of Stem Cell Aging by Metabolism and Epigenetics. *Cell Metab* **26**, 460-474 (2017).
75. Heneberg, P. Lactic Acidosis in Patients with Solid Cancer. *Antioxid Redox Signal* (2022).
76. Watson, M.J. & Delgoffe, G.M. Fighting in a wasteland: deleterious metabolites and antitumor immunity. *J Clin Invest* **132** (2022).
77. Bae, V.L. *et al.* Metastatic sublines of an SV40 large T antigen immortalized human prostate epithelial cell line. *The Prostate* **34**, 275-282 (1998).
78. Fedchenko, N. & Reifenrath, J. Different approaches for interpretation and reporting of immunohistochemistry analysis results in the bone tissue - a review. *Diagn Pathol* **9**, 221 (2014).
79. Zerbino, D.R., Wilder, S.P., Johnson, N., Juettemann, T. & Flicek, P.R. The ensembl regulatory build. *Genome biology* **16**, 56 (2015).
80. Trapnell, C. *et al.* Differential gene and transcript expression analysis of RNA-seq experiments

with TopHat and Cufflinks. *Nat Protoc* **7**, 562-578 (2012).
81. Nix, D.A., Courdy, S.J. & Boucher, K.M. Empirical methods for controlling false positives and estimating confidence in ChIP-Seq peaks. *BMC Bioinformatics* **9**, 523 (2008).
82. Zhao, Y. *et al.* Genetically encoded fluorescent sensors for intracellular NADH detection. *Cell Metab* **14**, 555-566 (2011).
83. Robinson, A.R. *et al.* Spontaneous DNA damage to the nuclear genome promotes senescence, redox imbalance and aging. *Redox Biol* **17**, 259-273 (2018).
84. Krzywinski, M. & Altman, N. POINTS OF SIGNIFICANCE Power and sample size. *Nat Methods* **10**, 1139-1140 (2013).

Acknowledgements

We are grateful to the members of Sun laboratory for reagents, comments and other contributions to this project. We thank Dr. Yongzhen Tao for thoughtful discussion of metabolic datasets. The work was supported by grants from National Key Research and Development Program of China (2020YFC2002800 and 2016YFC1302400 to Y.S.; 2019YFA0904800 to Y.Z.), National Natural Science Foundation of China (NSFC) (81472709, 31671425, 31871380, 82130045 to Y.S.; 32150030, 32030065, 32121005, 92049304 to Y.Z.; 81370730, 81571512 to Q.F.; 22007006 to G.Z.); the Strategic Priority Research Program of Chinese Academy of Sciences (XDB39010500) to Y.S.; Shanghai Municipal Science and Technology Commission Excellent Academic Leader Program (20XD1404300) to Y.S.; Anti-Ageing Collaborative Program of SIBS and BY-HEALTH (C01201911260006, C01202112160005 and C01202210146923) to Y.S.; the University and Locality Collaborative Development Program of Yantai (2019XDRHXMRC08 and 2020XDRHXMXK02 to Y.S.; 2021XDHZ082 to Q.F.); Natural Science Foundation of Shandong Province Joint Fund Program (ZR202108130049 and ZR2021LSW021) to Y.S.; the U.S. DoD PCRP (Idea Development Award PC111703) to Y.S.; Research Unit of New Techniques for Live-cell Metabolic Imaging (Chinese Academy of Medical Sciences, 2019-I2M-5-013 to Y.Z.), Innovative research team of high-level local universities in Shanghai (Y.Z.); Yantai Double Hundred Program to Q.F.; Taishan Scholars Construction Engineering (tsqn201909144), Special Project of Central Government for Local Science and Technology Development of Shandong Province (YDZX20203700001291) to G.Z.

Author contributions

Y.S. conceived this study, designed the experiments and orchestrated the project. X.D. performed most of the *in vitro* assays, part of the *in vivo* experiments and wrote part of the manuscript. Q.L and D.F. acquired and analyzed clinical samples from prostate and breast cancer patients, respectively, and managed subject information. S.L. and Y.Z. helped with metabolic profiling and GC-MS analysis of cell metabolites with SoNar- and FiLa-based genetically encoded fluorescence sensors. Q.X., Z.J. and X.R. performed some cell culture and drug treatment assays. G.Z. and X.W. rendered constructive advices. Q.F. performed partial preclinical studies and provided animal data. Q.L., J.C. and Y.Z. provided conceptual inputs and/or supervised a specific subset of experiments. Y.Z. organized the generation of SoNar- and FiLa-associated graphic illustrations. Y.S. performed data analysis, graphic presentation and finalized the manuscript. All authors critically read and commented on the final manuscript.

Competing interests

The authors declare no competing interests.

Inclusion & Ethics statement

All authors have agreed to all manuscript contents, the author list and its order and the author contribution statements. Any changes to the author list after submission will be subject to approval by all authors.

Additional information

Supplementary information The online version contains supplementary material available at specific link.

Correspondence and requests for materials should be addressed to Yu Sun.

Reprints and permissions information is available online.

Figure legends

Fig. 1. Genotoxicity induces senescence of human stromal cells which display upregulation of PDK4 and a full spectrum SASP.

a. Transcriptome-wide profiling of gene expression changes in primary normal human prostate stromal cell line PSC27 by microarray. Cell lysates were collected for analysis 7 d after treatment. CTRL, control. RAD, radiation. BLEO, bleomycin. HP, hydrogen peroxide. Red highlighted, typical soluble factors of the SASP. Microarray data adapted from Sun et al. with permission from *Nature Medicine*, copyright 2012, Springer Nature [21].

b. Quantitative RT-PCR to detect PDK4 expression after PSC27 cells were subject to individual treatment as indicated. Cell lysates were collected for measurement 7 d after establishment of stable cell sublines or completion of *in vitro* treatment. Signals normalized to CTRL. RS, replicative senescence. p16, lentiviral transduction of human tumor suppressor $p16^{INK4a}$. RAS, lentiviral transduction of human oncogene $HRAS^{G12V}$.

c. Immunoblot analysis of PDK4 expression in stromal cells as delineated in (**b**). GAPDH, loading control.

d. Comparative RT-PCR assay of PDK4 expression after treatment of PSC27 or prostate epithelial cells by agents as indicated. Cell lysates were collected for measurement 7 d after treatment. Signals normalized to CTRL. BPH1, M12, PC3, DU145, LNCaP and VCaP, human epithelial lines of prostate origin.

e. Comparative RT-PCR assay of PDK4 expression in human stromal cells 7 d after treatments performed as indicated. WI38, HFL1, HBF1203 and BJ, human stromal lines of different origins.

f. A time course RT-PCR assessment of the expression of PDK4 and a set of typical SASP factors (MMP1, WNT16B, SFRP2, SPINK1, MMP3, CXCL8, EREG, ANGPTL4 and AREG) after drug treatment of PSC27 cells *in vitro*. Numeric numbers indicate the individual days after treatment (indexed at the top line).

g. Immunoblot measurement of PDK4 expression at protein level at the individual timepoints as indicated. β-actin, loading control.

h. Comparative appraisal of human PDK family expression at transcript level in PSC27 cells after BLEO treatment. Signals normalized to untreated sample per gene. CXCL8, experimental control as a hallmark SASP factor.

i. Immunoblot assessment of the expression of PDK4 family members at protein level after BLEO treatment. β-actin, loading control.

Data are representative of 3 independent experiments. *P* values were calculated by Student's *t*-test (**b**, **e**, **f**, **h**) and one-way ANOVA (**d**). ^, $P > 0.05$. *, $P < 0.05$. **, $P < 0.01$. ***, $P < 0.001$. ****, $P < 0.0001$.

Fig. 2. Senescent cells display a glucose metabolic profile distinct from their normal and cancer counterparts.

a. A schematic molecular roadmap briefly outlining the landscape of glucose metabolism in mammalian cells.
b. Partial metabolic profiling (glycolysis) of senescent cells induced by BLEO (TIS) and incubated with uniformly labeled [U-$^{13}C_6$]-glucose. Results from gas chromatography-mass spectrometry (GC-MS) analysis of metabolites including DHAP, GAP, 3PG, pyruvate and lactate are shown.
c. Partial metabolic profiling (TCA cycle) of senescent cells induced by BLEO (TIS) and incubated with uniformly labeled [U-$^{13}C_6$]-glucose. Results from GC-MS analysis of metabolites including citrate, α-ketoglutarate, succinate, fumarate and malate, are presented. TCA, tricarboxylic acid cycle.
d. Heatmap depicting the changes of glucose catabolism-associated metabolites as measured for senescent cells by GC-MS.
e. Representative TEM images showing the ultrastructural profile of mitochondria in human stromal cells. L, low resolution. H, high resolution. Scale bars, 1.0 μm.
f. Measurement of extracellular fluids with XF24 extracellular flux analyzer. Pyruvate and lactate were assayed as indicated.
g. OCR of stromal cells was measured using an XF24 extracellular flux analyzer. Briefly, 1.5 μM oligomycin, 0.5 μM FCCP and 0.5 μM Rot/Ant were injected sequentially into each well. Glycolysis rate was calculated as (maximum rate measured before Oligo injection) minus (last rate measured before glucose injection). All Seahorse data were normalized with cell numbers, with metabolic parameters automatically calculated by WAVE software equipped in Seahorse. OCR, oxygen consumption rate. Oligo, oligomycin. FCCP, carbonyl cyanide 4-(trifluoromethoxy) phenylhydrazone. Rot, rotenone. Ant, antimycin. IN, PDK4-IN (PDK4 inhibitor, 10 nM)
h. Measurement of ATP production by stromal cells. ATP production was measured as (last rate measurement before Oligomycin injection) minus (minimum rate measurement after Oligomycin injection).
i. Assessment of basal respiration as an essential element of the senescence-associated metabolism program.
j. Examination of maximal respiration as another fundamental element of the senescence-associated metabolism program.
k. Assessment of non-mitochondrial oxygen consumption in stromal cells.
l. Measurement of pH values in stromal cells.
m. Determination of lactate production in stromal cells.
n. Examination of the leak of H+ (proton) from mitochondria of stromal cells.
Data in all bar plots are shown as mean ± SD and representative of 3 biological replicates.

P values were calculated by Student's *t*-test (**b, c, f, h-n**). ^, $P > 0.05$. * $P < 0.05$. ** $P < 0.01$. **** $P < 0.0001$.

Fig. 3. Senescent stromal cells display changes of NAD^+/NADH metabolism and are featured with PDK4-mediated production of lactate.

a. Measurement of glucose uptake of PSC27 cells upon senescence induction by therapeutic agents as indicated.
b. Examination of the pH value of human stromal cells treated as described in (**a**). Right inlet, representative images of conditioned media collected from proliferating and BLEO-induced senescent cells, respectively.
c. Schematic illustration of potential changes in cell metabolic activities specifically fluctuations of the NAD^+/NADH ratio during senescence induced by damaging insults.
d. Graphic model for design of SoNar, which is a fusion of cpYFP and the NADH-binding domain of T-Rex. Binding of NAD^+ or NADH induces changes in the protein conformation and fluorescence. Right, fluorescence ratios plotted against the NAD^+/NADH ratio at 400 μM total nicotinamide adenine dinucleotide. Fluorescence ratios were normalized to the control condition in the absence of nucleotides (n = 3).
e. Technical overview for *in vitro* imaging of living cells stably expressing the fluorescent sensor with confocal laser-scanning microscopy.
f. Excitation spectra of purified SoNar in the control condition (black), and after addition of 20 μM NAD^+ (green) or 20 μM NADH (orange), normalized to the peak intensity in the control condition. Emission was measured at 530 nm.
g. Fluorescence imaging of SoNar in proliferating (CTRL) or bleomycin-induced senescent (BLEO) PSC27 cells, in the absence or presence of PDK inhibitor (IN) for 2 h, Scale bar, 20 μm.
h. Quantification of SoNar or iNapc fluorescence in PSC27 cells (n = 30 cells). Left, SoNar. Right, iNapc.
i. Schematic representation of molecular design for lactate sensor FiLa. The fluorescent protein cpYFP was inserted into a monomer of the lactate-binding bacterial protein LldR. Binding of lactate induces changes in protein conformation and fluorescence. Right, Lactate titration curves of FiLa and FiLa-C sensors. Data are normalized to the initial value (n = 3).
j. Excitation spectra of purified FiLa in the control condition (black) and saturated with lactate (dark red). The excitation spectrum recorded at an emission wavelength of 530 nm has maxima at 425 and 490 nm. Data are normalized to peak intensity at 425 nm in the control condition.
k. Fluorescence imaging of FiLa or FiLa-C in CTRL and BLEO-induced senescent PSC27 cells, in the absence or presence of PDK inhibitor (IN) for 2 h, Scale bar, 20 μm.
l. Quantification of FiLa (left) and FiLa-C (right) fluorescence in PSC27 cells (n = 30 cells).

Data in all bar plots are shown as mean ± SD and representative of 3 biological replicates. *P* values were calculated by Student's *t*-test. ^, $P > 0.05$. * $P < 0.05$. ** $P < 0.01$. *** $P < 0.001$. **** $P < 0.0001$.

Fig. 4. Stromal expression of PDK4 induces profound changes of PCa cell expression profile and causes enhanced malignancy.

a. Heatmap depicting differentially expressed human transcripts in PCa lines including PC3, DU145 and M12 after a 3-d culture with the CM collected from PSC27 cells overexpressing PDK4 (PSC27-PDK4). In contrast to cancer cells cultured with control CM (PSC27-CTRL), the number of genes up- and downregulated *per* PCa line are indicated. The intensity of tracing lines are consistent with the relative expression fold change averaged *per* up- and downregulated genes.

b. Graphical visualization of pathways by GO profiling (pie chart depicting biological processes). Those significantly enriched genes in the upregulated list were sorted according to their fold change in PC3 cells exposed to the CM of PSC27-PDK4 cells.

c. Venn diagram displaying the overlap of transcripts co-upregulated in PC3, DU145 and M12 cells (*per* 2 or 3 lines) upon in culture treatment with the CM from PSC27-PDK4 stromal cells in contrast to those treated with the CM of PSC27-CTRL.

d. Summary of transcripts co-upregulated in PC3, DU145 and M12 lines (top ranked, with a fold change ≥ 5.0 and FDR < 0.01) upon treatment with the CM of PSC27-PDK4 stromal cells. Red highlighted, HTR2B.

e. Immunoblot assessment of protein expression of HTR2B in the three PCa lines. β-actin, loading control.

f. Measurement of the proliferation capacity of PCa lines at different conditions. As experimental group, human HTR2B was transduced into each PCa line, with LY 266097 applied to media as a drug treatment control.

g. Examination of the 2D migration activity of PCa lines at different conditions. Cells were treated in a manner similar to that described in (**f**).

h. Evaluation of the invasion ability of PCa lines at different conditions. Cells were treated in a manner similar to that described in (**f**).

i. Determination of the resistance of PCa lines to MIT upon exposure to the CM of PSC27-PDK4 stromal cells. MIT, mitoxantrone, a chemotherapeutic agent applied at the IC50 concentration *per* cell line established prior to the assay.

j. Dose-response curves (non-linear regression/curve fit) plotted from MIT-based viability assays of PC3 exposed to the CM of PSC27-PDK4 cells and treated by a range of concentrations of MIT.

Data in all bar plots are shown as mean ± SD. Data in **a**, **e-j** are representative of 3 independent experiments. All *P* values were calculated by Student's *t*-tests. ^, $P > 0.05$. *, $P < 0.05$. **, $P < 0.01$. ***, $P < 0.001$.

Fig. 5. Therapeutically targeting PDK4 in the damaged TME promotes therapeutic outcome in preclinical trials.

a. Schematic workflow of experimental procedure for severe combined immunodeficient (SCID) mice. Two weeks after subcutaneous implantation and *in vivo* uptake of tissue

recombinants, animals received either single or combinational agents administered as metronomic treatments composed of several cycles.

b. Statistical profiling of tumor end volumes. PC3 cells were xenograted alone or together with PSC27 cells to the hind flank of SCID mice. MIT and PDK4-IN was administered either alone or concurrently to induce tumor regression. Right, representative tumor images.

c. Transcript assessment of several canonical SASP factors expressed in stromal cells isolated from the tumors of SCID mice. Tissues from animals implanted with both stromal and cancer cells were subject to LCM isolation, total RNA preparation and expression assays. Note, the group measured as the lowest value was used as the normalization baseline *per* factor.

d. Representative IHC images of SA-β-Gal staining profile of tissues isolated from placebo or drug-treated animals. Scale bar, 100 μm.

e. Comparative statistics of SA-β-Gal staining for mouse tissues described in (**d**).

f. Statistical assessment of DNA-damaged and apoptotic cells in the tumor specimens analyzed in (**d**). Values are presented as percentage of cells positively stained by IHC with antibodies against γ-H2AX or caspase 3 (cleaved).

g. Representative IHC images of caspase 3 (cleaved) in tumors at the end of therapeutic regimens. Biopsies of placebo-treated animals served as negative controls for drug-treated mice. Scale bars, 100 μm.

h. Bulky disease-free survival plotted against the time of recombinant tissue injection until animal death attributed to the development of advanced bulky diseases. MS, median survival. *P* values were calculated by two-sided log-rank (Mantel–Cox) tests.

i. Measurement of circulating lactate in the peripheral blood of mice that underwent the therapeutic regimen involving MIT and/or PDK4-IN.

Data in all dot or bar graphs are shown as mean ± S.D. and representative of 3 independent experiments. All *P* values were calculated by Student's *t*-tests. ^, $P > 0.05$. *, $P < 0.05$. **, $P < 0.01$. ***, $P < 0.001$. ****, $P < 0.0001$.

Fig. 6. Lactate is a novel circulating biomarker indicative of *in vivo* SASP development and predicts adverse therapeutic outcome in cancer clinics.

a. Abundance of lactate in the serum of untreated and chemo-treated PCa patients. Data were derived from ELISA measurement and shown as mean ± SD. N = 20.

b. Abundance of CXCL8 protein in patient serum analyzed in (**a**). Data from ELISA assays and presented as mean ± SD. N = 20.

c. Abundance of SPINK1 protein in patient serum analyzed in (**a**). Data from ELISA assays and presented as mean ± SD. N = 20.

d. Scatterplot showing correlation between lactate and CXCL8 in the serum of individual patients described in (**a-c**). Pearson's correlation coefficient, *P* value and confidence interval are indicated.

e. Scatterplot showing correlation between lactate and SPINK1 in the serum of individual patients described in (**a-c**). Pearson's correlation coefficient, *P* value and confidence interval are indicated.

f. Heatmap depicting the overall correlation between serum lactate, stromal CXCL8,

serum CXCL8, stromal SPINK1 and serum SPINK1 in chemo-treated patients (n = 10). The raw scores of stromal CXCL8 and SPINK1 were derived from independent pathological reading of primary tumor tissues of PCa patients, with those of serum CXCL8 and SPINK1 obtained from ELISA assays. Color key, relative expression of these factors in stromal tissue or patient serum.

g. Kaplan-Meier survival analysis of chemo-treated PCa patients. Disease free survival (DFS) stratified according to circulating lactate in serum (low, average score < 2, dark green; high, average score ≥ 2, dark red). DFS represents the length (months) of period calculated from the date of chemotherapy to the point of first time disease relapse. Survival curves generated according to the Kaplan–Meier method, with *P* value calculated using a log-rank (Mantel-Cox) test. N = 10 per group.

h. TCGA data showing alterations of PDK4 in a variety of human cancer types at the genomic level, including mutation, amplification and deep deletion. Alteration frequency is displayed in percentage.

i. Graphic illustration to summarize metabolic reprogramming of senescent cells and formation of a lactate-enriched microenvironment in a genotoxic setting and functional implications of the metabolite lactate in promoting cancer resistance and potentially other age-related conditions.

Data in **a**-**e** are representative of 3 independent experiments. *P* values were calculated by Student's *t*-test (**a**-**c**), Pearson test (**d**-**e**) and log-rank (Mantel-Cox) test (**g**). ***, $P < 0.001$. ****, $P < 0.0001$.

Fig. 7. Lactate activates ROS production through inducing NOX1 expression and enhances the SASP intensity

a. Biochemical scheme illustrating intracellular mechanisms of ROS generation upon exposure of cells to lactate, a small molecule metabolite that can derive from either autocrine or paracrine pathways in the tissue microenvironment.

b. Examination of ROS biogenesis with 2'-7'-dichlorodihydrofluorescein diacetate (DCFH-DA), a cell permeable fluorescent probe sensitive to changes in cellular redox state. Experiments were performed 1 d after treatment of PSC27 cells with rotenone (10 μM), carbonyl cyanide 3-chlorophenylhydrazone (CCCP, 10 μM) and/or lactate (10 mM). Left, representative images. Scale bar, 10 μm. Right, statistics.

c. Immunoblot assay of representative NOX molecules and DDR signaling after exposure of cells to different treatments. β-actin, loading control.

d. Measurement of ROS production with DCFH-DA. Experiments were performed 1 d after treatment of BLEO-induced senescent PSC27 cells with ML-090, PDK4-IN and APX-115. Left, representative images. Scale bar, 10 μm. Right, statistics.

e. Confocal microscopy of immunofluorescence staining of PSC27 cells treated by BLEO and/or PDK4-IN. Primary antibodies against γH2AX and CXCL8 were employed. Scale bar, 10 μm.

f. Comparative statistics of DNA damage response (DDR) in PSC27 cells treated by agents as indicated in (**e**). DDR were classified into four sub-categories including 0 foci, 1-3 foci, 4-10 foci and >10 foci *per* cell.

g. Immunoblot analysis of the expression of target molecules after exposure of cells to different treatments. CXCL8, a hallmark SASP factor. β-actin, loading control.

h. Heatmap depicting the expression change pattern of genes in the transcriptome-wide range of PSC27 cells. The first 50 genes that were most upregulated upon BLEO treatment are shown, with their changes in the presence of PDK4-IN lined up correspondingly. Red stars, representative SASP factors. Data from each condition are presented in triplicates.

Data in **b**-**g** are representative of 3 independent experiments. *P* values were calculated by Student's *t*-test (**b**-**d**) or two-way ANOVA (**f**). ^, $P > 0.05$. *, $P < 0.05$. **, $P < 0.01$. ***, $P < 0.001$. ****, $P < 0.0001$.

Fig. 8. An intermittent PDK4-targeting regimen extends both healthspan and lifespan of aged animals.

a. Schematic design of physical functional examinations for 20-month-old C57BL/6J male mice receiving preclinical treatment by vehicle, PDK4-IN or PCC1 (biweekly) for consecutive 4 months. PCC1, senolytic control.

b. Representative images of SA-β-Gal staining of livers from young and aged mice treated with vehicle, PDK4-IN or PCC1 as described in (**a**). Scale bar, 200 μm.

c. Quantification and comparison of SA-β-Gal staining positivity in liver tissues as described in (**b**).

d. Quantification and comparison of SA-β-Gal staining positivity in lung tissues of experimental mice as described in (**a**).

e. Quantification and comparison of SA-β-Gal staining positivity in prostate tissues of experimental mice as described in (**a**).

f. Quantification and comparison of SA-β-Gal staining positivity in myocardium tissues of experimental mice as described in (**a**).

g. Representative haematoxylin and eosin (H&E) staining (left) and quantification of alveolar size (right) for the animals described in (**a**). Scale bar, 200 μm.

h. Quantitative measurement of maximal walking speed (relative to baseline) of experimental mice.

i-m. Quantitative measurement of maximal walking speed (relative to baseline) (**i**), performance time (**j**), grip strength (**k**), treadmill endurance (**l**) and daily activity (**m**) of 20-month-old experimental animals after the 4-month treatment.

n. Measurement of circulating lactate (in mM) in the peripheral blood of mice after the 4-month treatment as described in (**a**).

o. Schematic design for lifespan appraisal of mice (both sexes) at 24-27 months of age.

p. Post-treatment survival curves of C57BL/6J animals treated biweekly with vehicle (n = 68; 37 males, 31 females), PDK4-IN (n = 66; 33 males, 33 females) or PCC1 (n =67; 35 males, 32 females) starting at 24-27 months of age.

Male mice in each group were adapted in 3 (young) or 4 (aged) independent cages. For preclinical assays, n = 5/group for **c**-**f**, n = 10/group for **g**-**n**. Data in **b**-**n** are representative of 3 independent experiments. *P* values were calculated by Student's *t*-test (**c**-**f**, **g**-**n**) and log-rank (Mantel-Cox) test (**p**). ^, $P > 0.05$. *, $P < 0.05$. **, $P < 0.01$. ***, $P < 0.001$. ****, $P < 0.0001$.

Figures

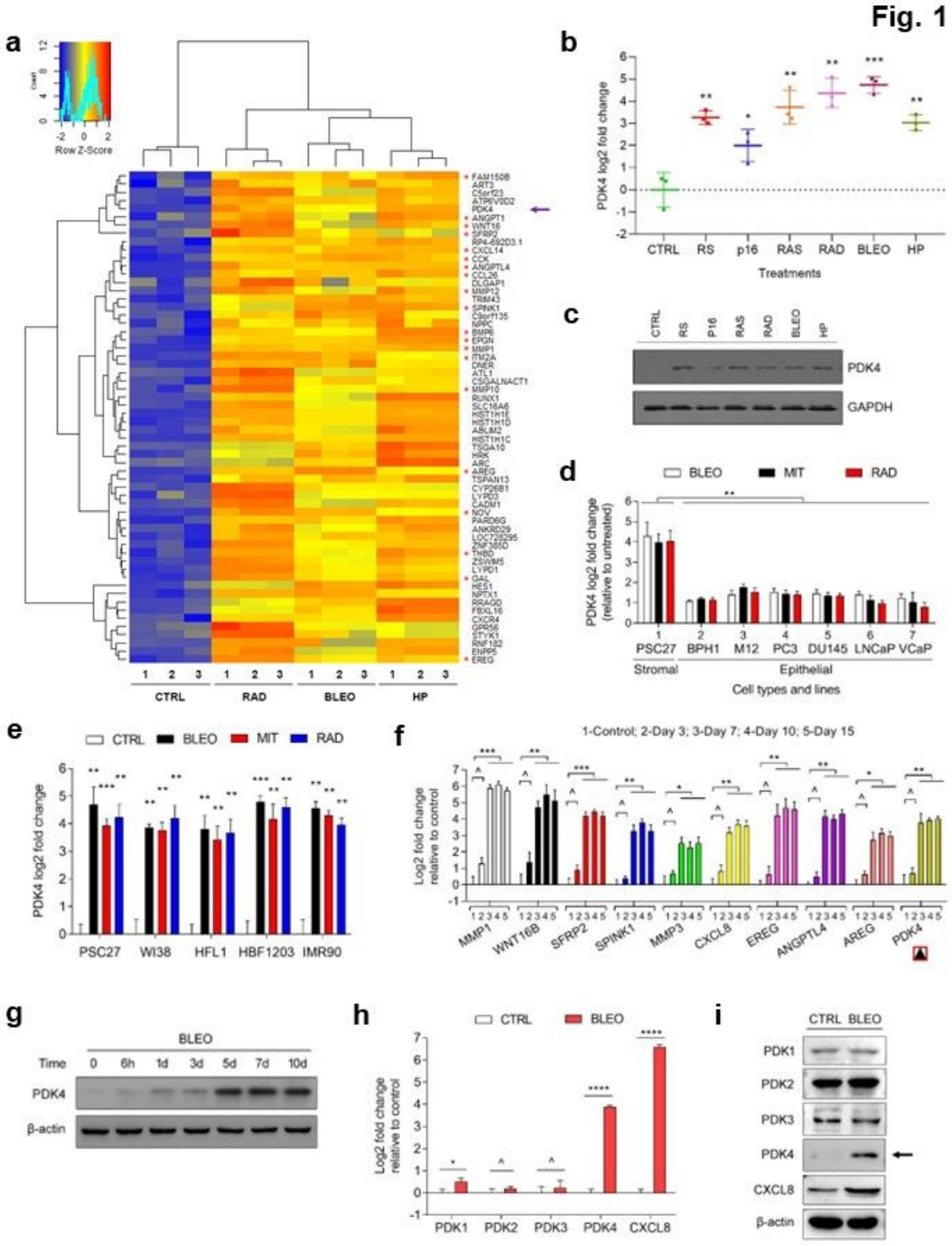

Figure 1

Genotoxicity induces senescence of human stromal cells which display upregulation of PDK4 and a full spectrum SASP. a. Transcriptome-wide profiling of gene expression changes in primary normal human prostate stromal cell line PSC27 by microarray. Cell lysates were collected for analysis 7 d after

treatment. CTRL, control. RAD, radiation. BLEO, bleomycin. HP, hydrogen peroxide. Red highlighted, typical soluble factors of the SASP. Microarray data adapted from Sun et al. with permission from Nature Medicine, copyright 2012, Springer Nature 21 . b. Quantitative RT-PCR to detect PDK4 expression after PSC27 cells were subject to individual treatment as indicated. Cell lysates were collected for measurement 7 d after establishment of stable cell sublines or completion of in vitro treatment. Signals normalized to CTRL. RS, replicative senescence. p16, lentiviral transduction of human tumor suppressor p16INK4a. RAS, lentiviral transduction of human oncogene HRASG12V . c. Immunoblot analysis of PDK4 expression in stromal cells as delineated in (b). GAPDH, loading control. d. Comparative RT-PCR assay of PDK4 expression after treatment of PSC27 or prostate epithelial cells by agents as indicated. Cell lysates were collected for measurement 7 d after treatment. Signals normalized to CTRL. BPH1, M12, PC3, DU145, LNCaP and VCaP, human epithelial lines of prostate origin. e. Comparative RT-PCR assay of PDK4 expression in human stromal cells 7 d after treatments performed as indicated. WI38, HFL1, HBF1203 and BJ, human stromal lines of different origins. f. A time course RT-PCR assessment of the expression of PDK4 and a set of typical SASP factors (MMP1, WNT16B, SFRP2, SPINK1, MMP3, CXCL8, EREG, ANGPTL4 and AREG) after drug treatment of PSC27 cells in vitro. Numeric numbers indicate the individual days after treatment (indexed at the top line). g. Immunoblot measurement of PDK4 expression at protein level at the individual timepoints as indicated. β-actin, loading control. h. Comparative appraisal of human PDK family expression at transcript level in PSC27 cells after BLEO treatment. Signals normalized to untreated sample per gene. CXCL8, experimental control as a hallmark SASP factor. i. Immunoblot assessment of the expression of PDK4 family members at protein level after BLEO treatment. β-actin, loading control. 54 Data are representative of 3 independent experiments. P values were calculated by Student’s t-test (b, e, f, h) and one-way ANOVA (d). ^, $P > 0.05$. *, $P < 0.05$. **, $P < 0.01$. ***, $P < 0.001$. ****, $P < 0.0001$.

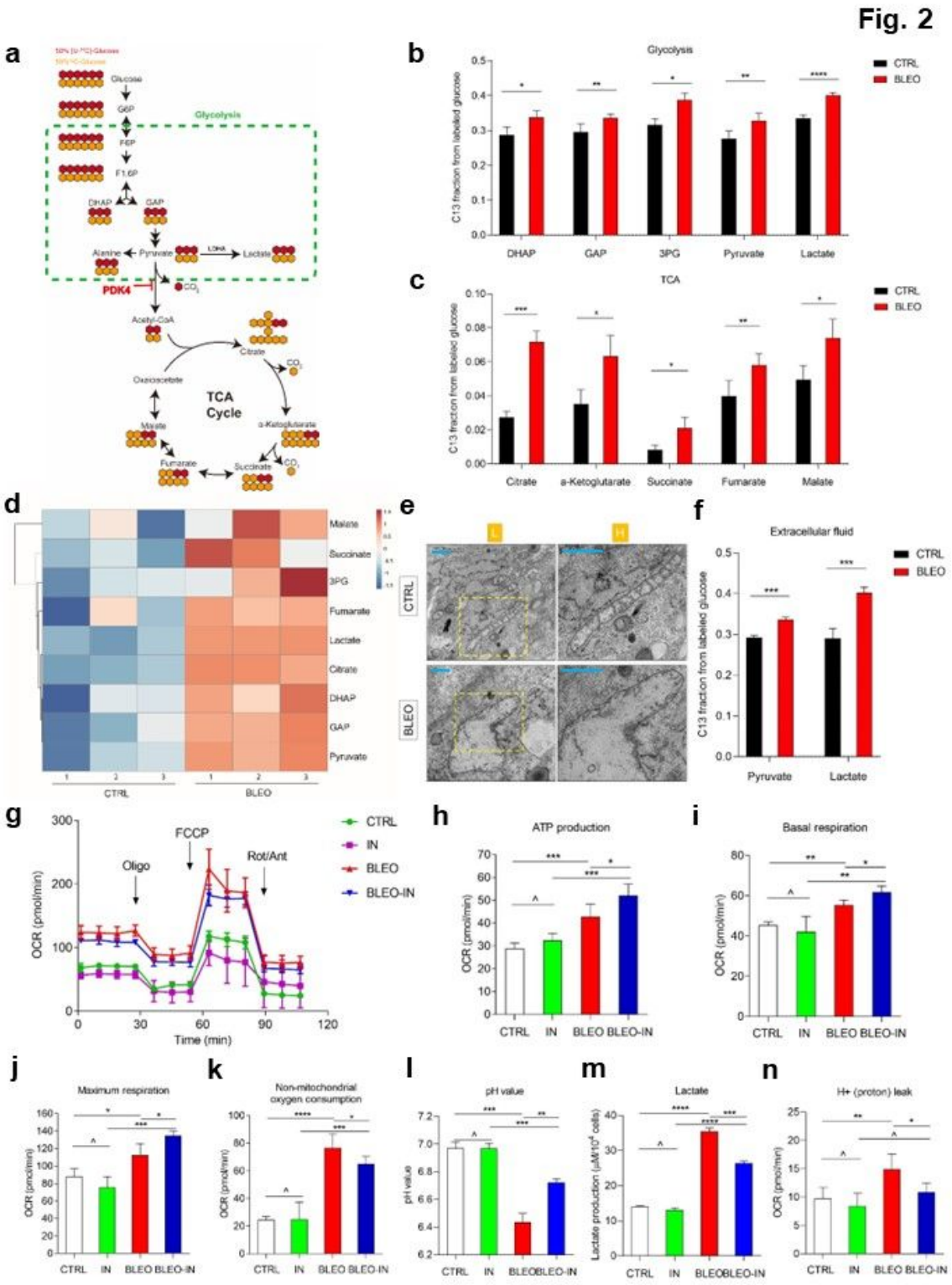

Figure 2

Senescent cells display a glucose metabolic profile distinct from their normal and cancer counterparts. a. A schematic molecular roadmap briefly outlining the landscape of glucose metabolism in mammalian cells. b. Partial metabolic profiling (glycolysis) of senescent cells induced by BLEO (TIS) and incubated with uniformly labeled [U13C6]-glucose. Results from gas chromatographymass spectrometry (GC-MS) analysis of metabolites including DHAP, GAP, 3PG, pyruvate and lactate are shown. c. Partial metabolic

profiling (TCA cycle) of senescent cells induced by BLEO (TIS) and incubated with uniformly labeled [U13C6]-glucose. Results from GC-MS analysis of metabolites including citrate, α-ketoglutarate, succinate, fumarate and malate, are presented. TCA, tricarboxylic acid cycle. d. Heatmap depicting the changes of glucose catabolism-associated metabolites as measured for senescent cells by GC-MS. e. Representative TEM images showing the ultrastructural profile of mitochondria in human stromal cells. L, low resolution. H, high resolution. Scale bars, 1.0 μm. f. Measurement of extracellular fluids with XF24 extracellular flux analyzer. Pyruvate and lactate were assayed as indicated. g. OCR of stromal cells was measured using an XF24 extracellular flux analyzer. Briefly, 1.5 μM oligomycin, 0.5 μM FCCP and 0.5 μM Rot/Ant were injected sequentially into each well. Glycolysis rate was calculated as (maximum rate measured before Oligo injection) minus (last rate measured before glucose injection). All Seahorse data were normalized with cell numbers, with metabolic parameters automatically calculated by WAVE software equipped in Seahorse. OCR, oxygen consumption rate. Oligo, oligomycin. FCCP, carbonyl cyanide 4-(trifluoromethoxy) phenylhydrazone. Rot, rotenone. Ant, antimycin. IN, PDK4-IN (PDK4 inhibitor, 10 nM) h. Measurement of ATP production by stromal cells. ATP production was measured as (last rate measurement before Oligomycin injection) minus (minimum rate measurement after Oligomycin injection). i. Assessment of basal respiration as an essential element of the senescence-associated metabolism program. j. Examination of maximal respiration as another fundamental element of the senescenceassociated metabolism program. k. Assessment of non-mitochondrial oxygen consumption in stromal cells. l. Measurement of pH values in stromal cells. m. Determination of lactate production in stromal cells. n. Examination of the leak of H+ (proton) from mitochondria of stromal cells. Data in all bar plots are shown as mean ± SD and representative of 3 biological replicates. 55 P values were calculated by Student's t-test (b, c, f, h-n). ^, $P > 0.05$. * $P < 0.05$. ** $P < 0.01$. **** $P < 0.0001$.

Fig. 3

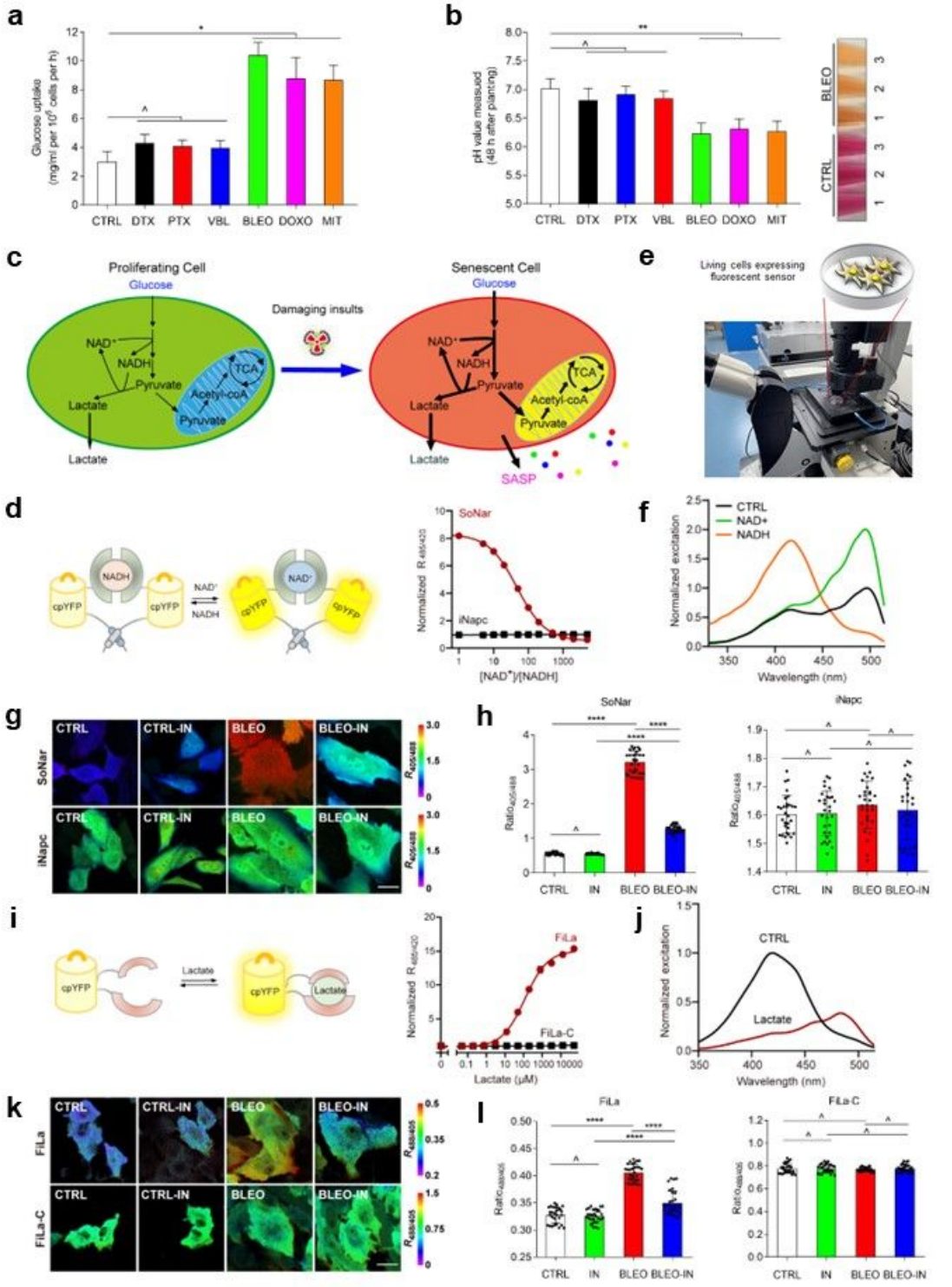

Figure 3

Senescent stromal cells display changes of NAD+ /NADH metabolism and are featured with PDK4-mediated production of lactate. a. Measurement of glucose uptake of PSC27 cells upon senescence induction by therapeutic agents as indicated. b. Examination of the pH value of human stromal cells treated as described in (a). Right inlet, representative images of conditioned media collected from proliferating and BLEO-induced senescent cells, respectively. c. Schematic illustration of potential

changes in cell metabolic activities specifically fluctuations of the NAD+ /NADH ratio during senescence induced by damaging insults. d. Graphic model for design of SoNar, which is a fusion of cpYFP and the NADH-binding domain of T-Rex. Binding of NAD+ or NADH induces changes in the protein conformation and fluorescence. Right, fluorescence ratios plotted against the NAD+ /NADH ratio at 400 μM total nicotinamide adenine dinucleotide. Fluorescence ratios were normalized to the control condition in the absence of nucleotides (n = 3). e. Technical overview for in vitro imaging of living cells stably expressing the fluorescent sensor with confocal laser-scanning microscopy. f. Excitation spectra of purified SoNar in the control condition (black), and after addition of 20 μM NAD+ (green) or 20 μM NADH (orange), normalized to the peak intensity in the control condition. Emission was measured at 530 nm. g. Fluorescence imaging of SoNar in proliferating (CTRL) or bleomycin-induced senescent (BLEO) PSC27 cells, in the absence or presence of PDK inhibitor (IN) for 2 h, Scale bar, 20 μm. h. Quantification of SoNar or iNapc fluorescence in PSC27 cells (n = 30 cells). Left, SoNar. Right, iNapc. i. Schematic representation of molecular design for lactate sensor FiLa. The fluorescent protein cpYFP was inserted into a monomer of the lactate-binding bacterial protein LldR. Binding of lactate induces changes in protein conformation and fluorescence. Right, Lactate titration curves of FiLa and FiLa-C sensors. Data are normalized to the initial value (n = 3). j. Excitation spectra of purified FiLa in the control condition (black) and saturated with lactate (dark red). The excitation spectrum recorded at an emission wavelength of 530 nm has maxima at 425 and 490 nm. Data are normalized to peak intensity at 425 nm in the control condition. k. Fluorescence imaging of FiLa or FiLa-C in CTRL and BLEO-induced senescent PSC27 cells, in the absence or presence of PDK inhibitor (IN) for 2 h, Scale bar, 20 μm. l. Quantification of FiLa (left) and FiLa-C (right) fluorescence in PSC27 cells (n = 30 cells). Data in all bar plots are shown as mean ± SD and representative of 3 biological replicates. P values were calculated by Student’s t-test. ^, P > 0.05. * P < 0.05. ** P < 0.01. *** P < 0.001. **** P < 0.0001.

Fig. 4

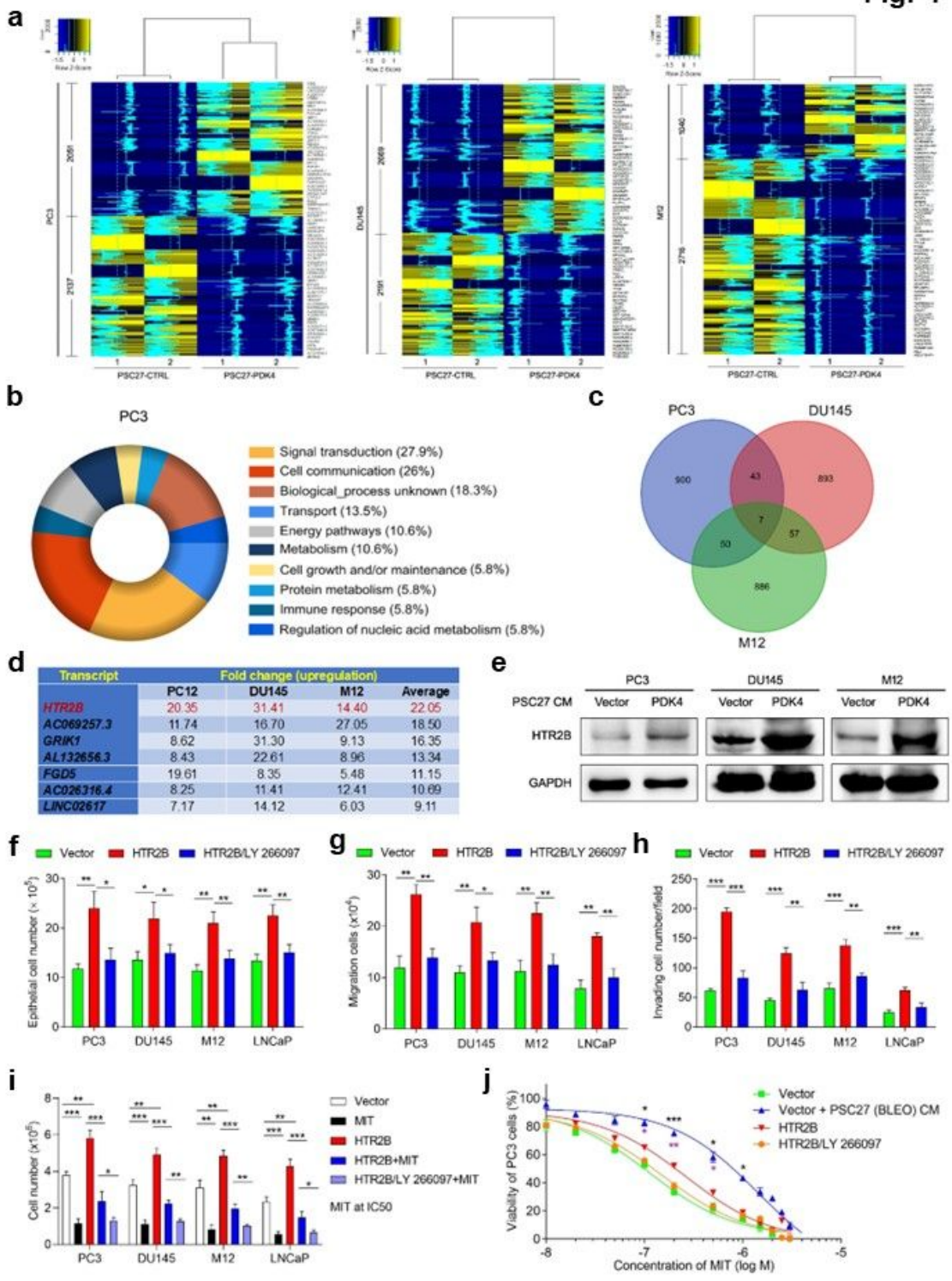

Figure 4

Stromal expression of PDK4 induces profound changes of PCa cell expression profile and causes enhanced malignancy. a. Heatmap depicting differentially expressed human transcripts in PCa lines including PC3, DU145 and M12 after a 3-d culture with the CM collected from PSC27 cells overexpressing PDK4 (PSC27-PDK4). In contrast to cancer cells cultured with control CM (PSC27-CTRL), the number of genes up- and downregulated per PCa line are indicated. The intensity of tracing lines are consistent with

the relative expression fold change averaged per up- and downregulated genes. b. Graphical visualization of pathways by GO profiling (pie chart depicting biological processes). Those significantly enriched genes in the upregulated list were sorted according to their fold change in PC3 cells exposed to the CM of PSC27-PDK4 cells. c. Venn diagram displaying the overlap of transcripts co-upregulated in PC3, DU145 and M12 cells (per 2 or 3 lines) upon in culture treatment with the CM from PSC27-PDK4 stromal cells in contrast to those treated with the CM of PSC27-CTRL. d. Summary of transcripts co-upregulated in PC3, DU145 and M12 lines (top ranked, with a fold change ≥ 5.0 and FDR < 0.01) upon treatment with the CM of PSC27-PDK4 stromal cells. Red highlighted, HTR2B. e. Immunoblot assessment of protein expression of HTR2B in the three PCa lines. β-actin, loading control. f. Measurement of the proliferation capacity of PCa lines at different conditions. As experimental group, human HTR2B was transduced into each PCa line, with LY 266097 applied to media as a drug treatment control. g. Examination of the 2D migration activity of PCa lines at different conditions. Cells were treated in a manner similar to that described in (f). h. Evaluation of the invasion ability of PCa lines at different conditions. Cells were treated in a manner similar to that described in (f). i. Determination of the resistance of PCa lines to MIT upon exposure to the CM of PSC27- PDK4 stromal cells. MIT, mitoxantrone, a chemotherapeutic agent applied at the IC50 concentration per cell line established prior to the assay. j. Dose-response curves (non-linear regression/curve fit) plotted from MIT-based viability assays of PC3 exposed to the CM of PSC27-PDK4 cells and treated by a range of concentrations of MIT. Data in all bar plots are shown as mean ± SD. Data in a, e-j are representative of 3 independent experiments. All P values were calculated by Student's t-tests. ^, P > 0.05. *, P < 0.05. **, P < 0.01. ***, P < 0.001.

Fig. 5

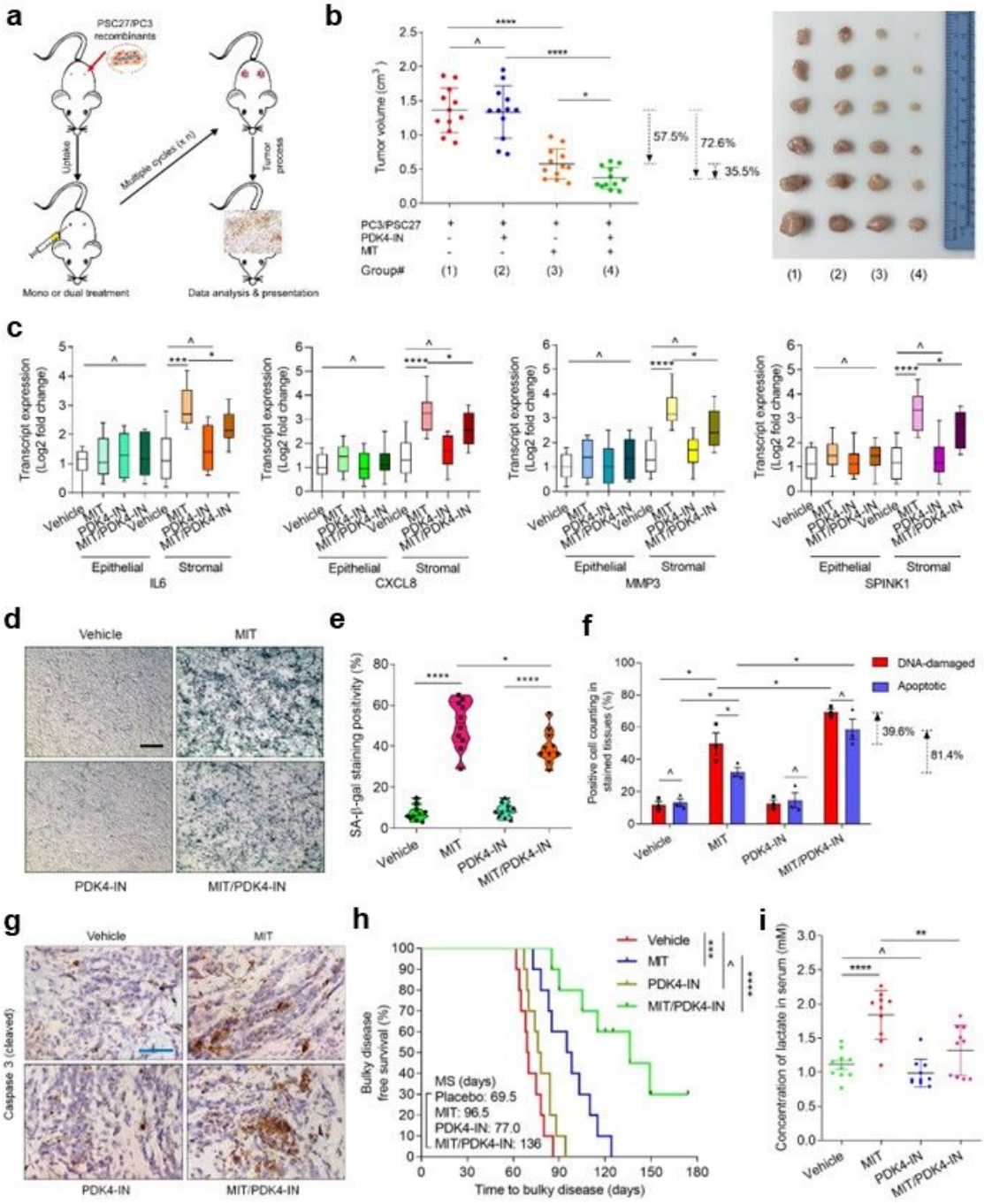

Figure 5

Therapeutically targeting PDK4 in the damaged TME promotes therapeutic outcome in preclinical trials. a. Schematic workflow of experimental procedure for severe combined immunodeficient (SCID) mice. Two weeks after subcutaneous implantation and in vivo uptake of tissue 57 recombinants, animals received either single or combinational agents administered as metronomic treatments composed of several cycles. b. Statistical profiling of tumor end volumes. PC3 cells were xenograted alone or together

with PSC27 cells to the hind flank of SCID mice. MIT and PDK4-IN was administered either alone or concurrently to induce tumor regression. Right, representative tumor images. c. Transcript assessment of several canonical SASP factors expressed in stromal cells isolated from the tumors of SCID mice. Tissues from animals implanted with both stromal and cancer cells were subject to LCM isolation, total RNA preparation and expression assays. Note, the group measured as the lowest value was used as the normalization baseline per factor. d. Representative IHC images of SA-β-Gal staining profile of tissues isolated from placebo or drug-treated animals. Scale bar, 100 μm. e. Comparative statistics of SA-β-Gal staining for mouse tissues described in (d). f. Statistical assessment of DNA-damaged and apoptotic cells in the tumor specimens analyzed in (d). Values are presented as percentage of cells positively stained by IHC with antibodies against γ-H2AX or caspase 3 (cleaved). g. Representative IHC images of caspase 3 (cleaved) in tumors at the end of therapeutic regimens. Biopsies of placebo-treated animals served as negative controls for drugtreated mice. Scale bars, 100 μm. h. Bulky disease-free survival plotted against the time of recombinant tissue injection until animal death attributed to the development of advanced bulky diseases. MS, median survival. P values were calculated by two-sided log-rank (Mantel–Cox) tests. i. Measurement of circulating lactate in the peripheral blood of mice that underwent the therapeutic regimen involving MIT and/or PDK4-IN. Data in all dot or bar graphs are shown as mean ± S.D. and representative of 3 independent experiments. All P values were calculated by Student's t-tests. ^, $P > 0.05$. *, $P < 0.05$. **, $P < 0.01$. ***, $P < 0.001$. ****, $P < 0.0001$.

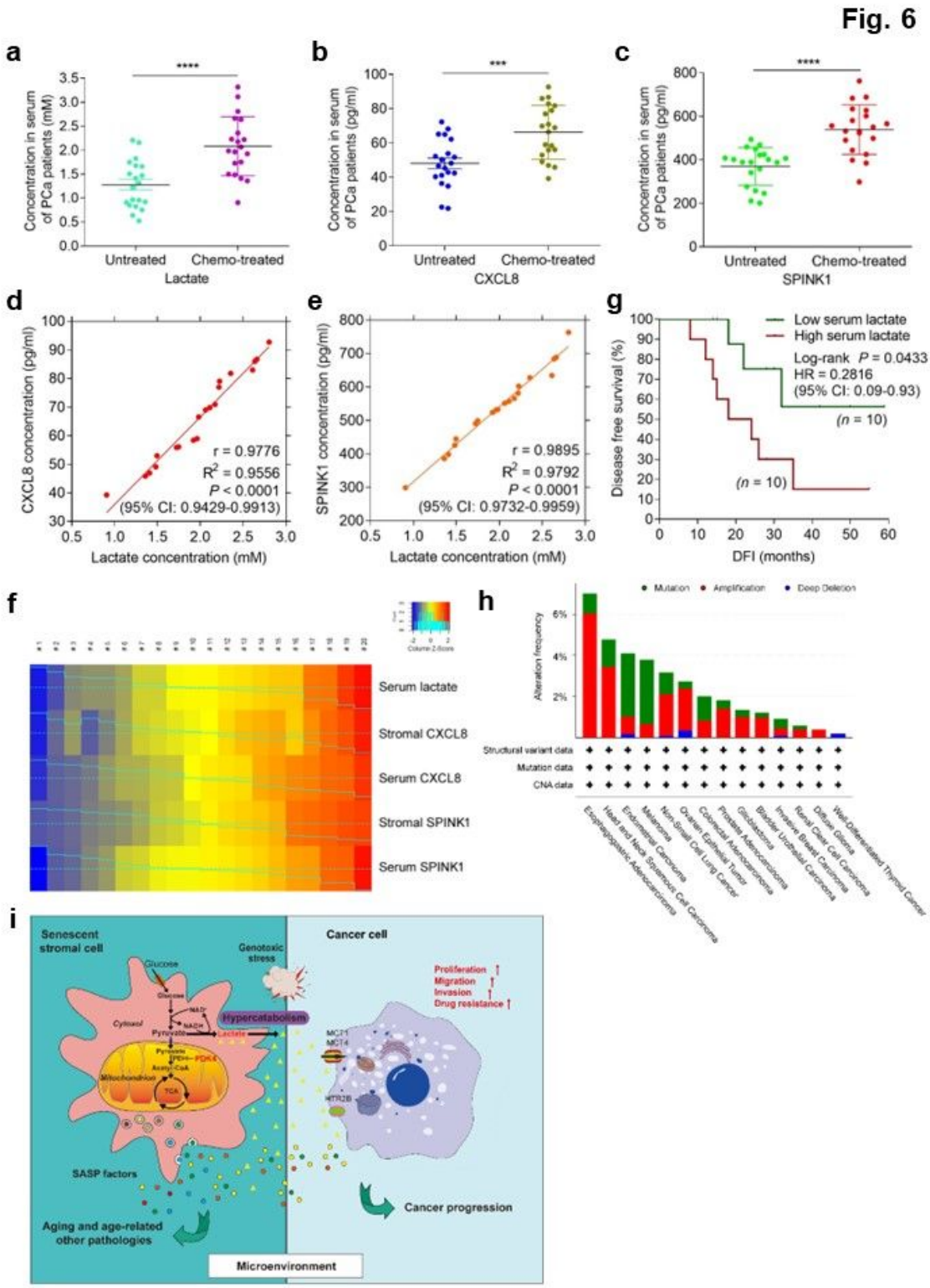

Figure 6

Lactate is a novel circulating biomarker indicative of in vivo SASP development and predicts adverse therapeutic outcome in cancer clinics. a. Abundance of lactate in the serum of untreated and chemo-treated PCa patients. Data were derived from ELISA measurement and shown as mean ±SD. N = 20. b. Abundance of CXCL8 protein in patient serum analyzed in (a). Data from ELISA assays and presented as mean ±SD. N = 20. c. Abundance of SPINK1 protein in patient serum analyzed in (a). Data from ELISA

assays and presented as mean ±SD. N = 20. d. Scatterplot showing correlation between lactate and CXCL8 in the serum of individual patients described in (a-c). Pearson's correlation coefficient, P value and confidence interval are indicated. e. Scatterplot showing correlation between lactate and SPINK1 in the serum of individual patients described in (a-c). Pearson's correlation coefficient, P value and confidence interval are indicated. f. Heatmap depicting the overall correlation between serum lactate, stromal CXCL8, 58 serum CXCL8, stromal SPINK1 and serum SPINK1 in chemo-treated patients (n = 10). The raw scores of stromal CXCL8 and SPINK1 were derived from independent pathological reading of primary tumor tissues of PCa patients, with those of serum CXCL8 and SPINK1 obtained from ELISA assays. Color key, relative expression of these factors in stromal tissue or patient serum. g. Kaplan-Meier survival analysis of chemo-treated PCa patients. Disease free survival (DFS) stratified according to circulating lactate in serum (low, average score < 2, dark green; high, average score ≥ 2, dark red). DFS represents the length (months) of period calculated from the date of chemotherapy to the point of first time disease relapse. Survival curves generated according to the Kaplan–Meier method, with P value calculated using a log-rank (Mantel-Cox) test. N = 10 per group. h. TCGA data showing alterations of PDK4 in a variety of human cancer types at the genomic level, including mutation, amplification and deep deletion. Alteration frequency is displayed in percentage. i. Graphic illustration to summarize metabolic reprogramming of senescent cells and formation of a lactate-enriched microenvironment in a genotoxic setting and functional implications of the metabolite lactate in promoting cancer resistance and potentially other age-related conditions. Data in a-e are representative of 3 independent experiments. P values were calculated by Student's t-test (a-c), Pearson test (d-e) and log-rank (Mantel-Cox) test (g). ***, P < 0.001. ****, P < 0.0001.

Fig. 7

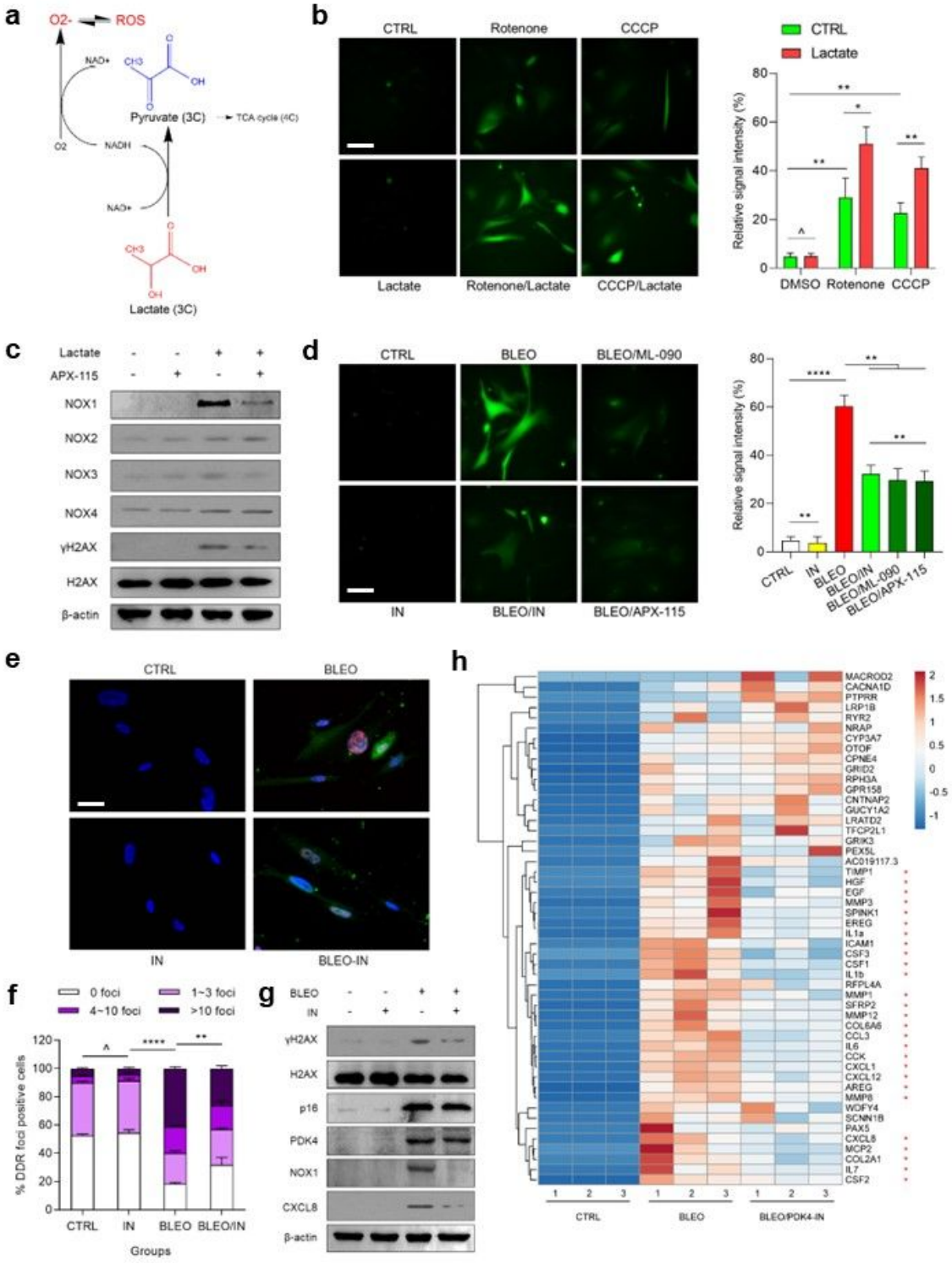

Figure 7

Lactate activates ROS production through inducing NOX1 expression and enhances the SASP intensity a. Biochemical scheme illustrating intracellular mechanisms of ROS generation upon exposure of cells to lactate, a small molecule metabolite that can derive from either autocrine or paracrine pathways in the tissue microenvironment. b. Examination of ROS biogenesis with 2'-7'-dichlorodihydrofluorescein diacetate (DCFH-DA), a cell permeable fluorescent probe sensitive to changes in cellular redox state.

Experiments were performed 1 d after treatment of PSC27 cells with rotenone (10 μM), carbonyl cyanide 3-chlorophenylhydrazone (CCCP, 10 μM) and/or lactate (10 mM). Left, representative images. Scale bar, 10 μm. Right, statistics. c. Immunoblot assay of representative NOX molecules and DDR signaling after exposure of cells to different treatments. β-actin, loading control. d. Measurement of ROS production with DCFH-DA. Experiments were performed 1 d after treatment of BLEO-induced senescent PSC27 cells with ML-090, PDK4-IN and APX-115. Left, representative images. Scale bar, 10 μm. Right, statistics. e. Confocal microscopy of immunofluorescence staining of PSC27 cells treated by BLEO and/or PDK4-IN. Primary antibodies against γH2AX and CXCL8 were employed. Scale bar, 10 μm. f. Comparative statistics of DNA damage response (DDR) in PSC27 cells treated by agents as indicated in (e). DDR were classified into four sub-categories including 0 foci, 1-3 foci, 4-10 foci and >10 foci per cell. g. Immunoblot analysis of the expression of target molecules after exposure of cells to different treatments. CXCL8, a hallmark SASP factor. β-actin, loading control. 59 h. Heatmap depicting the expression change pattern of genes in the transcriptome-wide range of PSC27 cells. The first 50 genes that were most upregulated upon BLEO treatment are shown, with their changes in the presence of PDK4-IN lined up correspondingly. Red stars, representative SASP factors. Data from each condition are presented in triplicates. Data in b-g are representative of 3 independent experiments. P values were calculated by Student's t-test (b-d) or two-way ANOVA (f). ^, $P > 0.05$. *, $P < 0.05$. **, $P < 0.01$. ***, $P < 0.001$. ****, $P < 0.0001$.

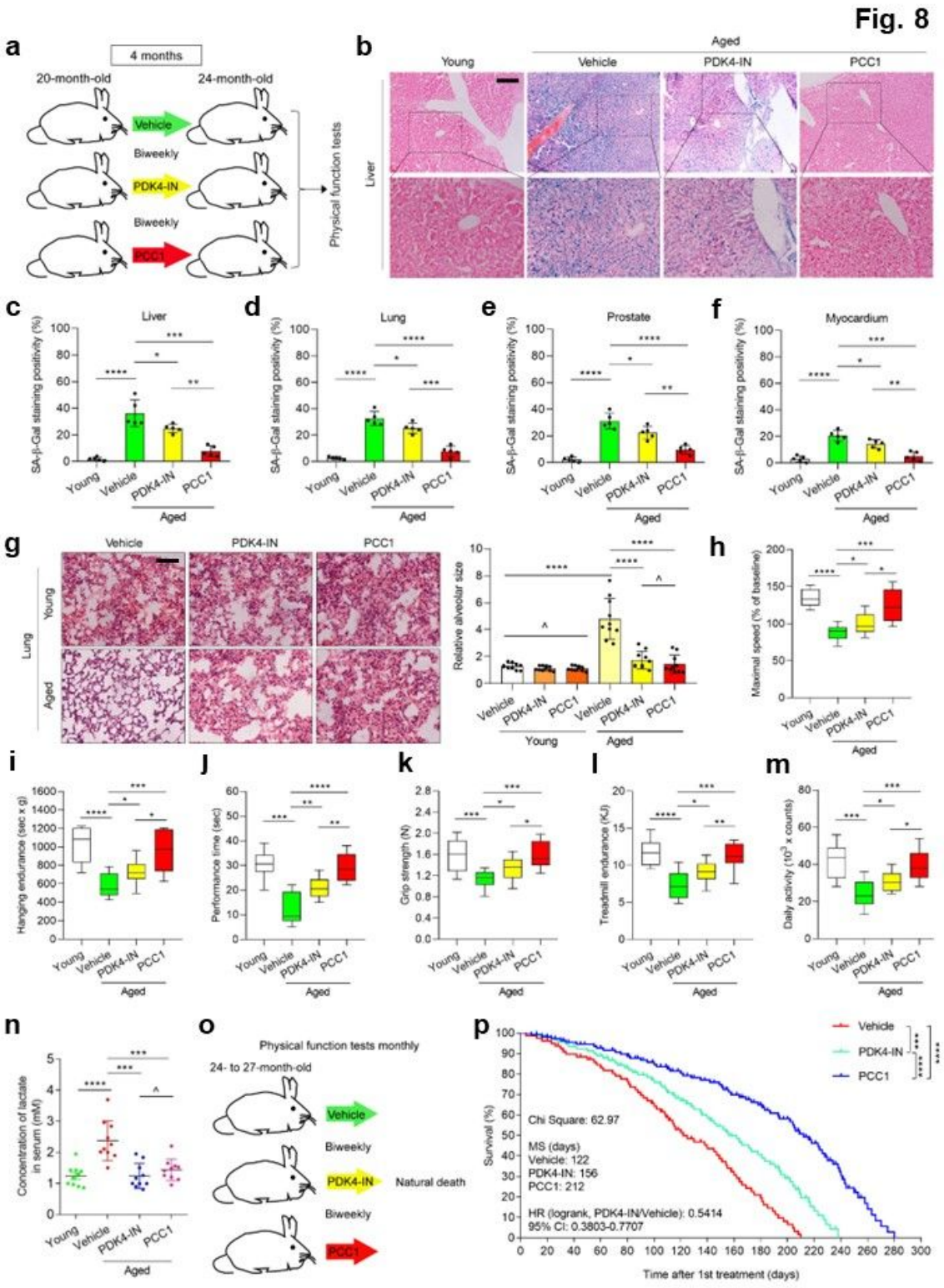

Figure 8

An intermittent PDK4-targeting regimen extends both healthspan and lifespan of aged animals. a. Schematic design of physical functional examinations for 20-month-old C57BL/6J male mice receiving preclinical treatment by vehicle, PDK4-IN or PCC1 (biweekly) for consecutive 4 months. PCC1, senolytic control. b. Representative images of SA-β-Gal staining of livers from young and aged mice treated with vehicle, PDK4-IN or PCC1 as described in (a). Scale bar, 200 μm. c. Quantification and comparison of SA-

β-Gal staining positivity in liver tissues as described in (b). d. Quantification and comparison of SA-β-Gal staining positivity in lung tissues of experimental mice as described in (a). e. Quantification and comparison of SA-β-Gal staining positivity in prostate tissues of experimental mice as described in (a). f. Quantification and comparison of SA-β-Gal staining positivity in myocardium tissues of experimental mice as described in (a). g. Representative haematoxylin and eosin (H&E) staining (left) and quantification of alveolar size (right) for the animals described in (a). Scale bar, 200 μm. h. Quantitative measurement of maximal walking speed (relative to baseline) of experimental mice. i-m. Quantitative measurement of maximal walking speed (relative to baseline) (i), performance time (j), grip strength (k), treadmill endurance (l) and daily activity (m) of 20-month-old experimental animals after the 4-month treatment. n. Measurement of circulating lactate (in mM) in the peripheral blood of mice after the 4-month treatment as described in (a). o. Schematic design for lifespan appraisal of mice (both sexes) at 24-27 months of age. p. Post-treatment survival curves of C57BL/6J animals treated biweekly with vehicle (n = 68; 37 males, 31 females), PDK4-IN (n = 66; 33 males, 33 females) or PCC1 (n =67; 35 males, 32 females) starting at 24-27 months of age. Male mice in each group were adapted in 3 (young) or 4 (aged) independent cages. For preclinical assays, n = 5/group for c-f, n = 10/group for g-n. Data in b-n are representative of 3 independent experiments. P values were calculated by Student's t-test (c-f, g-n) and log-rank (Mantel-Cox) test (p). ^, P > 0.05. *, P < 0.05. **, P < 0.01. ***, P < 0.001. ****, P < 0.0001.

Supplementary Files

This is a list of supplementary files associated with this preprint. Click to download.

- ExtendedDatafigurelegends.docx
- SupplementaryInformationall.pdf
- PDK4extendeddata02.ppt